Seismotectonic framework of the 2010 February 27 M_w 8.8 Maule, Chile earthquake sequence

Gavin P. Hayes,[1] Eric Bergman,[2] Kendra L. Johnson,[1,3] Harley M. Benz,[1] Lucy Brown[4] and Anne S. Meltzer[4]

[1] *National Earthquake Information Center, United States Geological Survey, Golden, CO 80401, USA. E-mail: ghayes@usgs.gov*
[2] *Global Seismological Services, Golden, CO 80401, USA*
[3] *Department of Geophysics, Colorado School of Mines, Golden, CO 80401, USA*
[4] *Department of Earth and Environmental Sciences, Lehigh University, Bethlehem, PA 18015, USA*

GJI Seismology

SUMMARY

After the 2010 M_w 8.8 Maule earthquake, an international collaboration involving teams and instruments from Chile, the US, the UK, France and Germany established the International Maule Aftershock Deployment temporary network over the source region of the event to facilitate detailed, open-access studies of the aftershock sequence. Using data from the first 9-months of this deployment, we have analyzed the detailed spatial distribution of over 2500 well-recorded aftershocks. All earthquakes have been relocated using a hypocentral decomposition algorithm to study the details of and uncertainties in both their relative and absolute locations. We have computed regional moment tensor solutions for the largest of these events to produce a catalogue of 465 mechanisms, and have used all of these data to study the spatial distribution of the aftershock sequence with respect to the Chilean megathrust. We refine models of co-seismic slip distribution of the Maule earthquake, and show how small changes in fault geometries assumed in teleseismic finite fault modelling significantly improve fits to regional GPS data, implying that the accuracy of rapid teleseismic fault models can be substantially improved by consideration of existing fault geometry model databases. We interpret all of these data in an integrated seismotectonic framework for the Maule earthquake rupture and its aftershock sequence, and discuss the relationships between co-seismic rupture and aftershock distributions. While the majority of aftershocks are interplate thrust events located away from regions of maximum co-seismic slip, interesting clusters of aftershocks are identified in the lower plate at both ends of the main shock rupture, implying internal deformation of the slab in response to large slip on the plate boundary interface. We also perform Coulomb stress transfer calculations to compare aftershock locations and mechanisms to static stress changes following the Maule rupture. Without the incorporation of uncertainties in earthquake locations, just 55 per cent of aftershock nodal planes align with faults promoted towards failure by co-seismic slip. When epicentral uncertainties are considered (on the order of just ±2–3 km), 90 per cent of aftershocks are consistent with occurring along faults demonstrating positive stress transfer. These results imply large sensitivities of Coulomb stress transfer calculations to uncertainties in both earthquake locations and models of slip distributions, particularly when applied to aftershocks close to a heterogeneous fault rupture; such uncertainties should therefore be considered in similar studies used to argue for or against models of static stress triggering.

Key words: Earthquake source observations; Seismicity and tectonics; Subduction zone processes; South America.

1. INTRODUCTION

On 2010 February 27, at 06:34:14 UTC (03:34 at the epicentre), the M_w 8.8 Maule earthquake ruptured a ~400+ km long section of the South American subduction zone in south-central Chile [epicentral location 36.12°S, 72.90°W, depth 22 km; US Geological Survey (USGS), National Earthquake Information Center (NEIC), http://on.doi.gov/yKhpUb]. The earthquake occurred along the subduction interface separating the Nazca and South American plates, where oceanic lithosphere of the Nazca Plate obliquely subducts

beneath South America at a rate of approximately 7.4 cm yr^{-1} (DeMets *et al.* 2010). This event caused extensive damage in nearby coastal cities and excited a large near- and far-field tsunami, the former of which caused localized run-up as high as 29 m near Constitución (Fritz *et al.* 2011). Aftershocks of the earthquake (through 2010 December) covered an area approximately 700×300 km^2 in size, overlapping the northern extent of the great 1960 M_w 9.5 Chile earthquake to the south, and the southern extent of the 1985 M 8.2 Central Chile earthquake to the north (Fig. 1).

Before the Maule earthquake, the plate interface extending ∼150 km south of the main shock hypocentre, which had been referred to as the South Central Chile seismic gap (McCann *et al.* 1979; Campos *et al.* 2002; Ruegg *et al.* 2009), had not slipped coseismically in a large earthquake since a M 8.5 megathrust earthquake in 1835 (Figs 1 and 2). The region north of the hypocentre, on the other hand, had partially failed during large earthquakes in 1906 (M 8.4), 1928 (M 8.0) and in 1985 (M 8.2) (e.g. Beck *et al.* 1998). Recent geodetic studies reveal that the plate interface between 38.0°S to 35.5°S was nearly fully locked during the 6 yr period from 1996 to 2002 (Ruegg *et al.* 2009; Moreno *et al.* 2010).

The USGS W-phase (Kanamori & Rivera 2008; Hayes *et al.* 2009; Duputel *et al.* 2011; Deputel *et al.* 2012) centroid moment tensor (CMT) solution (http://on.doi.gov/z5LHcG) indicates the earthquake ruptured a shallow thrust fault that aligns well with the geometry of the slab up-dip of the hypocentre (Fig. 1), with a best double-couple fault plane of strike $\varphi = 016°$, dip $\delta = 14°$, and rake $\lambda = 104°$. The solution of the global centroid moment tensor project (GCMT; http://www.globalcmt.org, Ekström *et al.* 2012) has a seismic moment of $mo = 1.86 \times 10^{29}$ dyne-cm, in close agreement with the W-phase moment, though with a slightly steeper dip ($\delta = 18°$). These solutions indicate that this earthquake, at the time, represented the fifth largest event recorded during the modern era of instrumental seismology (eclipsed since by the 2011 March 11, M_w 9.0 Tohoku earthquake; Hayes 2011; Hayes *et al.* 2011, http://on.doi.gov/X4d1J1).

In the weeks following this earthquake, an unprecedented international collaboration involving teams and instruments from Chilean Universities; the Incorporated Research Institutions for Seismology (IRIS) in the US; the Institut National des Sciences de l'Univers of the Centre National de la Recherche Scientifique (INSU, CNRS) in France; Geo Forschungs Zentrum Posdam (GFZ) in Germany; and the University of Liverpool in the UK, was established to deploy the International Maule Aftershock Deployment (IMAD) temporary network. Over 160 mostly broadband sensors were deployed over the on-land extent of the earthquake source region (Fig. 1). Data from almost all of these stations were made available immediately following their collection through IRIS and GFZ, spanning 2010 March–December.

These data have been scanned through a regional, offline implementation of the NEIC processing system (Hydra; Buland *et al.* 2009) in simulated real time, identifying over 30 000 events in the ∼9 month time period. Of these, 2375 well-recorded events have been analyzed in greater detail, handpicking waveforms to improve location and depth constraint. Regional moment tensors (RMTs) have been computed for 465 events of M_w 3.6 and above, where data quality and azimuthal coverage were good enough to produce well-constrained mechanisms. Finally, regional phases from these events were added to teleseismic observations and relocated using a hypocentral decomposition (HDC) algorithm to produce a higher quality catalogue of 1080 earthquakes, a subset of the 2088 events discussed above. This stepwise approach allows us to interpret all of these data sets within a consistent, regionally anchored framework.

The main contribution of this study is the compilation of a high-resolution, relocated aftershock catalogue for the 2010 February 27, M_w 8.8 Maule earthquake, complete with absolute horizontal and vertical uncertainties, and with associated and co-located RMTs for a large subset of the database. We also go on to use the catalogue to characterize the tectonic framework of the earthquake sequence. Using the relocated main shock hypocentre, we update the USGS finite fault model (http://on.doi.gov/yVUcUQ), based on further detailed analysis of input data and arrival times, revised fault plane geometry (using Slab1.0, Hayes *et al.* 2012), and a thorough exploration of the inversion model space. We analyze the surface deformation predicted by this model, and compare this to available geodetic and coastal geologic post-earthquake observations, to help constrain improvements in our inversion models. We examine the Coulomb stress transfer predicted by the event resolved both onto the slab interface and also onto the nodal planes of the aftershock RMTs. By subdividing our RMT catalogue based on the tectonic setting of each event in the upper, lower or interplate environment, we discuss the spatial distribution of aftershocks with respect to main shock slip and resulting regions of increased stress, and use this information to analyze how aftershocks responded to the main shock rupture.

2. PREVIOUS STUDIES OF THE AFTERSHOCK SEQUENCE

Since the collection of the IMAD data, several published studies have analyzed the spatial distribution and basic tectonic framework of the aftershock sequence. We discuss several major studies here—two that have produced catalogues of the aftershock sequence from automatic picking of the data set (e.g. Lange *et al.* 2012; Rietbrock *et al.* 2012), and a third which analyzes aftershock source processes using a selection of regional and teleseismic moment tensors (Agurto *et al.* 2012).

Through the automatic picking and processing of the first 6 months of IMAD data, Lange *et al.* (2012) located over 20 000 aftershocks in the source region of the Maule earthquake. They identify several distinct tectonic settings active during this period: (1) earthquakes in a region they call the outer rise, outboard of the subduction zone and adjacent to the main shock rupture; (2) plate interface seismicity in or adjacent to the regions of highest co-seismic slip; (3) seismicity in a cluster at the deeper limit of interface seismogenesis below the main shock rupture zone, and thus likely associated with after-slip; (4) earthquakes at intermediate (80–120 km) depths, within the subducting slab; and (5) earthquakes in the upper plate at the northern end of the rupture along crustal faults oblique to the subduction zone, associated with two major normal faulting aftershocks on 2010 March 11. These authors note that comparisons between aftershock locations and slip are dependent on the slip model used in the comparison—in other words, reliability of the source inversion procedure and thus of the resulting model is an important factor in studying such correlations. Comparisons of their aftershock catalogue to the Vigny *et al.* (2011) model show aftershock activity predominantly down-dip of the regions of highest co-seismic slip.

The Rietbrock *et al.* (2012) study also uses automated picking and processing algorithms, and builds a catalogue of over 30 000 earthquakes occurring over just the first 2 months of the IMAD deployment. This study also attempts to improve upon the accuracy of automated detection algorithms by incorporating *S*-wave arrivals, and by using a 2-D velocity model. Resulting locations from the
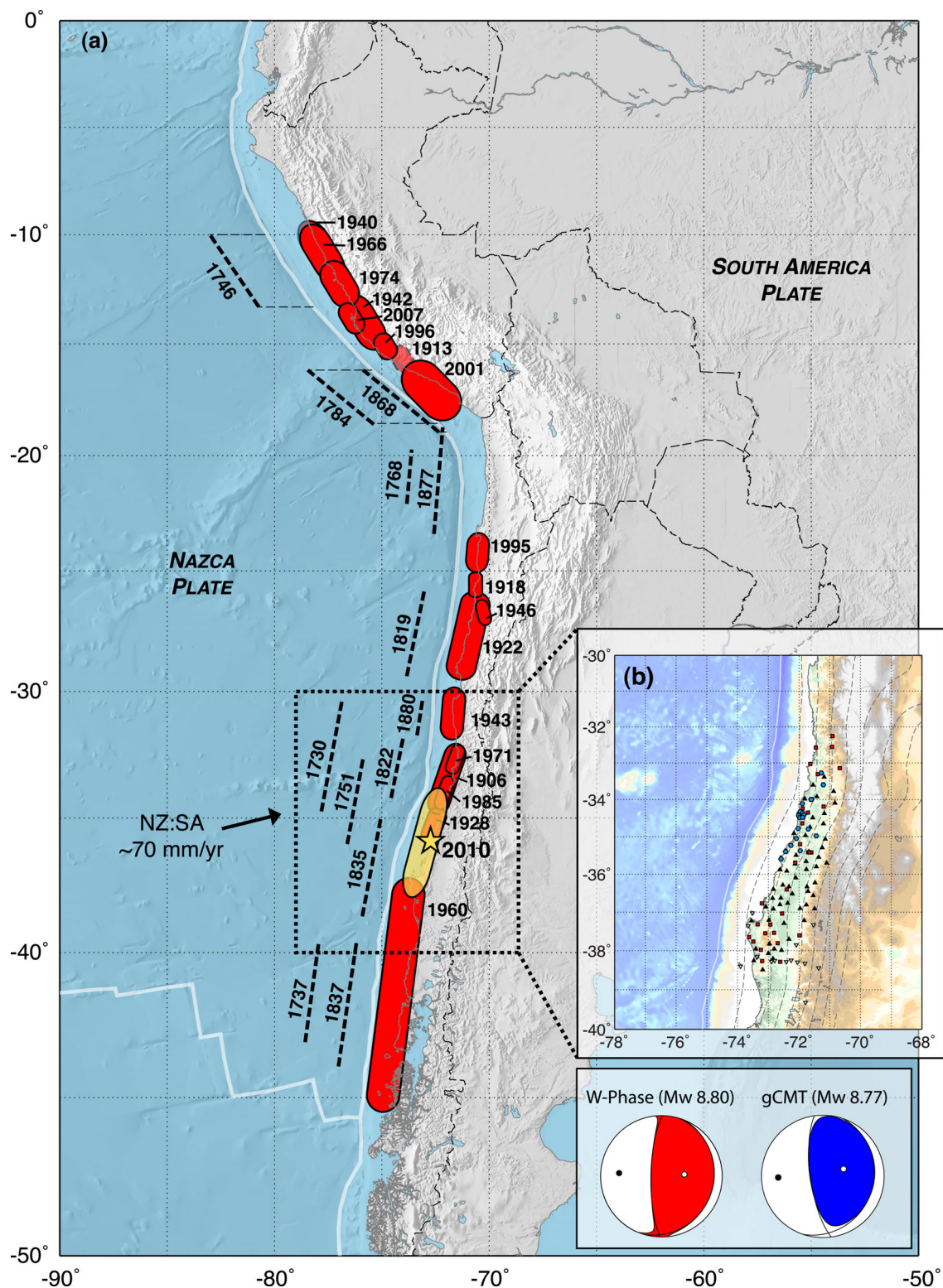
Figure 1. Tectonic setting of the 2010 February 27 M_w 8.8 Maule earthquake. (a) The seismologic history of the South America subduction zone; major 20th century ruptures are shown with red polygons representing their approximate rupture extent, following Beck *et al.* (1998). Approximate rupture lengths of major pre-20th century earthquakes since the 18th century are shown with black dashed lines outboard of the subduction zone for clarity (Beck *et al.* 1998, and references therein). The extent of the 2010 rupture is illustrated with a yellow polygon; the star represents the earthquake epicentre. CMT mechanisms for the main shock are given in the inset. The black arrow represents Nazca: South America Plate motion of approximately 70 mm yr⁻¹. The dashed black box shows the extent of all subsequent figures, and of (b), which shows stations from the IMAD aftershock deployment. Different symbols represent the operating institution; black triangles are IRIS (US) stations, inverted white triangles UK, red squares French, and blue hexagons German. Slab1.0 model contours are shown with dashed grey lines (Hayes *et al.* 2012). Background bathymetric data, here and in subsequent figures, is taken from the GEBCO_08 grid, version 20100927, http://www.gebco.net).
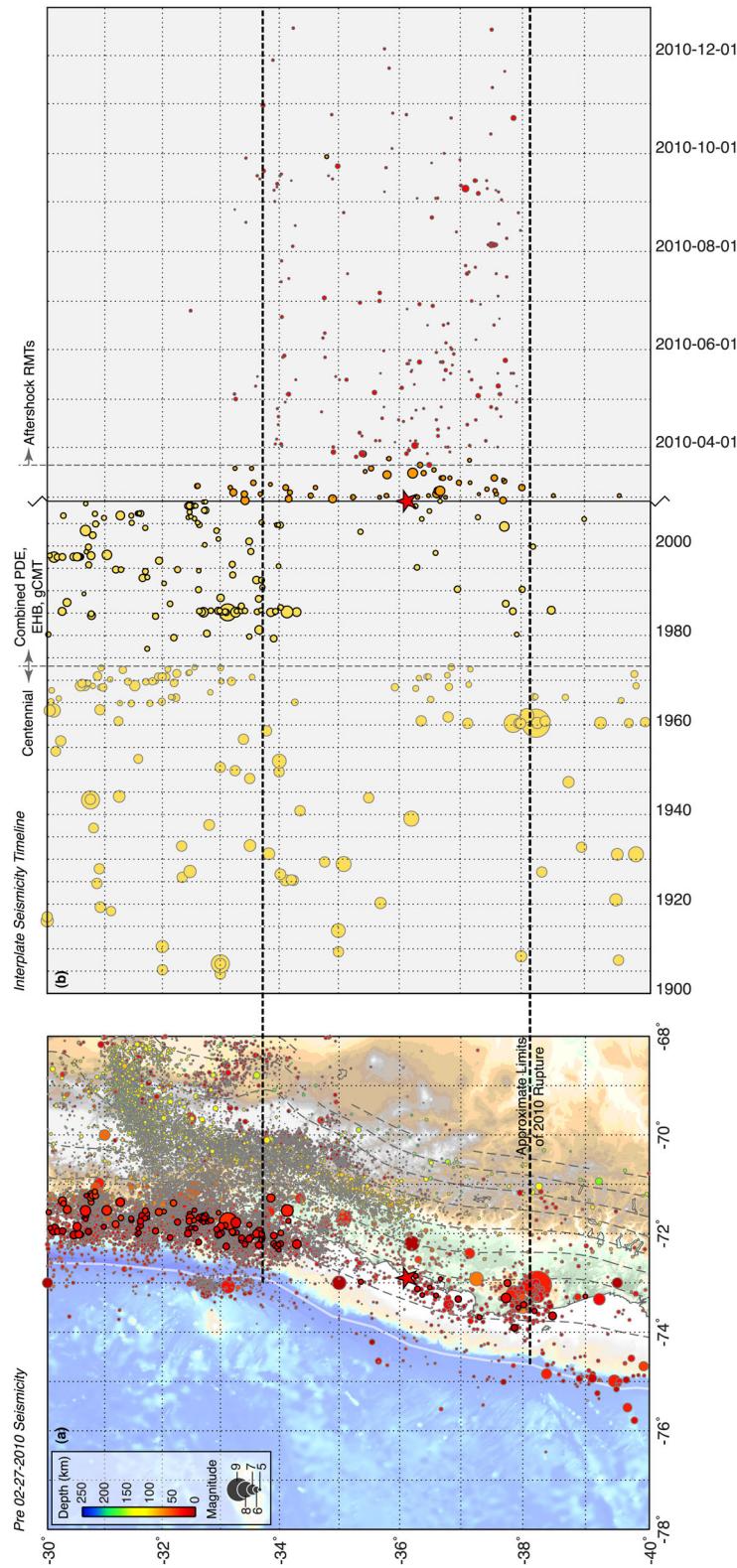
Figure 2. (a) Pre 2010 February 27 seismicity in the centennial (Engdahl & Villeseñor 2002; plotted 1900–1973), EHB (Engdahl *et al.* 1998; plotted 1964–present) and USGS PDE (plotted 1973–present, for those events without EHB locations) catalogues. Earthquake symbols are sized by magnitude and coloured by depth. Those shown with thicker black outlines represent interplate earthquakes, discriminated via a comparison of their hypocentres and associated GCMT mechanisms to the Slab1.0 subduction zone model for the region (see text for details). Slab1.0 model contours are shown with dashed grey lines. The location of the February 27, 2010 epicentre is shown with a star. Approximate rupture limits (based on aftershock seismicity) are illustrated with dashed black lines. In (b), we show a timeline of centennial catalogue (pre-1976) and interplate seismicity (post-1976, the beginning of the GCMT catalogue) in the source region of the Maule earthquake, showing the relative quiescence of the rupture area prior to the 2010 rupture. Yellow circles with light grey outlines are centennial catalogue events; yellow circles with thicker black outlines are EHB/PDE/GCMT catalogue interface events. Orange circles represent post-main shock events from the PDE catalogue, while red circles represent aftershocks used in this study. Both of these later two data sets have also been filtered according to either their GCMT (for PDE/orange events) or RMT (for regional aftershocks/red events) mechanism to identify interplate earthquakes.

Rietbrock catalogue agree well with those from Lange *et al.* (2012), identifying aftershock activity outboard of the subduction zone with the oceanic plate, in two distinct clusters along the subduction zone thrust, and within the upper plate surrounding the Pichilemu region, where the 2010 March 11 normal faulting aftershocks occurred. This study goes on to use aftershock distributions to discriminate between slip models of varying quality, based on the assumption that aftershocks should generally occur in areas of rapid transition between high and low slip, surrounding (but not co-located with) areas of high slip. Under such a premise, the slip model of Vigny *et al.* (2011) is preferred over those of (for example) Lorito *et al.* (2011) and Delouis *et al.* (2010), because aftershocks locate at the down-dip extent of shallow high-slip regions, rather than somewhat coincident with highest slip. Their findings support a model where aftershocks occur predominantly in the transitional regions between high and low slip, rather than preferentially in areas of lowest slip.

Agurto *et al.* (2012) build on the catalogue produced by Rietbrock *et al.* (2012), analyzing the largest events to produce a catalogue of approximately 125 RMT solutions. They also relocate CMT solutions from the global CMT catalogue (http://www.globalcmt.org), adding almost 150 further moment tensors to their data set. Using this catalogue, they infer that most large aftershocks (70 per cent) occur on the subduction thrust interface. Like Rietbrock *et al.* (2012), Agurto *et al.* (2012) conclude that such events occur predominantly away from the areas of highest co-seismic slip, based on comparisons to the slip model of Moreno *et al.* (2012). Interestingly, they also note that, in contrast to their findings for large events, small ($M < 4$) aftershocks predominantly occur where co-seismic slip is highest, possibly as a result of processes occurring in the damage zone around the megathrust interface.

These studies highlight the importance of precise aftershock locations and source inversions for subsequent analyses—whether these are direct comparisons of the two data, interpretations of tectonic settings of aftershocks, Coulomb stress transfer modelling, or other studies. Single-event locations are particularly sensitive to traveltime calculations for offshore ray-paths in these studies (since this is where the majority of events occur), leading to large uncertainties in earthquake locations when azimuthal coverage is limited, as is the case when locating offshore events. This problem can be mitigated by using multiple-event location techniques. We perform multiple-event relocations and address in detail issues of accuracy in this study, and discuss the implications of our results for the types of comparisons discussed above.

3. AUTOMATICALLY PICKING THE IMAD DATA SET

All of the portable seismic waveform data processed as part of this study were run through the same processing system used by NEIC in its real-time operations. These data were played back through the NEIC high-frequency waveform picker and associator in order to efficiently form initial locations and magnitudes for the suite of earthquakes they recorded. Once this process was completed, a list of earthquakes were reviewed with the highest priority being the analysis of the largest earthquakes, approximately M < 4 or larger. We restricted the processing to regional distances because we could easily combine the regional parametric data with the previously reviewed results from NEIC operations, eliminating the need to duplicate the NEIC review process. Once completed, the list of aftershocks from the processing of the temporary stations was compared against the NEIC preliminary determination of epicentres

(PDE) bulletin to make sure that no larger aftershocks were missing that were located teleseismically by NEIC. Out of the more than 3000 events reviewed, we found that the automatic system missed only about 15 or fewer larger events.

The NEIC automatic processing system computes a wide range of network-averaged high-frequency magnitudes and long-period magnitudes that follow the International Association of Seismology and Physics of the Earth's Interior (IASPEI) magnitude conventions. Since our automatic processing of the temporary seismic data was restricted to regional distances, we only computed M_d, M_l and M_w based on waveform modelling of regional phases following procedures described in Herrmann *et al.* (2011a). Most of the larger events (M5.5 or larger) had well-determined teleseismic moment tensor solutions; consequently, the M_w processing of the temporary seismic data concentrated on determining RMT solutions for events primarily in the magnitude range of M 3.5 to 5.5 (see Section 5 below).

The regional earthquake locations were determined using AK135 spherical earthquake reference velocity model (Kennett *et al.* 1995). This model was chosen in order to maintain consistency with NEIC real-time and bulletin operations, which use the same velocity model. The final earthquake locations using the hypocentrodial decomposition from the combined teleseismic and regional phase data, discussed in the next section, also used the AK135 velocity model.

4. EARTHQUAKE RELOCATIONS

The method of location calibration we employ is based on multiple event location using HDC (Jordan & Sverdrup 1981). Although there are several algorithms in use for obtaining improved relative locations through multiple event relocation (e.g. joint hypocentral determination, Dewey 1972; double difference, Waldhauser & Ellsworth 2000), HDC is uniquely suitable for calibrated location studies because it naturally separates the location problem into two parts, the relative locations of clustered events and the absolute location (hypocentroid) of the cluster as a whole. This allows us to select the data and apply weighting specifically for these two estimation problems in such a way as to optimize the resolution of relative locations and produce a minimally biased estimate of the location of the cluster as a whole. This is not true of the majority of other earthquake relocation algorithms, which in general only provide improved relative locations, often without any measure of location uncertainty. Our method has been extensively tested against standard single-event location codes such as the Engdahl-Van der Hilst-Buland algorithm (EHB; Engdahl *et al.* 1998), other multiple event relocation techniques (e.g. Rodi *et al.* 2002), and has been applied in a number of seismo-tectonic studies (e.g. Walker *et al.* 2005; Tatar *et al.* 2007; Bondar *et al.* 2008; Walker *et al.* 2011; Ghods *et al.* 2012).

For the relocation analysis, the Maule data set is split into 15 subclusters based on latitudinal extent, each containing 150–200 events, to maintain manageable matrix sizes in the singular value decompositions that are performed in each inversion. Each subcluster is relocated independently, except that in a few cases we carried over some events from neighboring subclusters that were especially well recorded locally and also well-recorded teleseismically—such events help provide essential 'connectivity' between the local, regional and teleseismic data sets.

The hypocentroid of each subcluster is located using only local-distance P and S readings. For the Maule subclusters, we were able to obtain stable estimates of the hypocentroid using arrivals

at no more than 0.6–0.8° epicentral distance. Most of those raypaths are onshore. We use a custom 1-D layered crustal model for traveltime calculations at local and regional distances (based on the fit to observed phase arrivals from the calibrated locations). The short path lengths of the readings used to determine the hypocentroids of the subclusters ensure minimal location bias of the hypocentroid from unmodelled velocity variations. Cluster vectors, which establish the relative location of each event with respect to the cluster hypocentroid, are estimated using nearly all-available arrival time data, regardless of phase type or epicentral distance. This is possible because relative locations are determined from arrival time differences that are insensitive to baseline errors in the theoretical traveltime model. Theoretical arrival times and derivatives for teleseismic phases are calculated from the global 1-D model AK135 (Kennett *et al.* 1995).

Our relocation and calibration methodology departs from standard practice in dealing with outlier arrival time readings by emphasizing consistency between repeated readings (of a given phase from different events in a cluster to the same station) rather than assessing the size of residuals against some reference traveltime model. A considerable amount of work goes into estimation of what we refer to as 'empirical reading errors' from the specific arrival time data set. This estimate is based on a robust estimator of spread (Croux & Rousseeuw 1992) applied to the traveltime residuals for a specific station and phase. The estimate of spread makes no assumption about the underlying distribution and requires no estimate of central location. A minimum value of 0.15 s is normally enforced to avoid numerical instability.

In addition to their use in weighting the arrival time data for inversion, we also use empirical reading errors to detect outliers in the data, which are flagged. Because outlier readings can cause good readings to have large residuals, the process needs to be done incrementally, starting with the largest residuals, to avoid rejection of good data. We gradually remove the largest outliers, followed by relocation, until the normalized, de-meaned distribution of each station-phase approaches a Gaussian distribution. This 'cleaning' process is repeated until the traveltime residuals satisfy a 3σ criterion, using the current empirical reading error as the estimate of σ, and is crucial in providing a self-consistent statistical framework for estimating location uncertainties.

The effect of systematic and comprehensive estimation of empirical reading errors and associated outlier rejection is that the arrival time data set is reduced to one that more closely approaches the assumption of zero-mean, normally distributed data which underlies the estimation of improved locations and their uncertainties. This process is essential in providing uncertainties in both relative and absolute earthquake locations, a product that is absent in most other earthquake relocation techniques. Gross errors are still possible from, for example, misidentified phases, incorrectly associated readings, incorrect station locations, and temporary equipment or operational problems at stations. Tests against ground truth seismic sources in other studies using the same methodology, such as clusters composed of nuclear tests, show that our procedures provide estimates of epicentral location accuracy that are perhaps underestimated by about 1 km.

To relocate each earthquake, we combined phase readings from our manual picking of regional data, discussed above, with teleseismic phase readings from the NEIC's earthquake data record (EDR). The data set is thus quite heterogeneous. For the main shock and early aftershocks, before the temporary stations were deployed, the data set consists of larger earthquakes recorded only at the small number of permanent regional stations, and teleseismically. Most

such events occurred offshore. During the time when the temporary stations were in place, many of the events in our data set were recorded only by local and regional stations. The most important of these are the events that occurred onshore, such that good azimuthal coverage at local distances is obtained. Some onshore events did occur during the period in which many temporary stations were operational that were also large enough to be observed at teleseismic distances. These are the most important events in our data set, since they provide the linkage between onshore events whose locations can be determined accurately with local data, and the large offshore events that account for the vast majority of seismic moment release. Through this linkage the locations of the offshore events can be estimated with the same accuracy as those events recorded with local observations on land.

Each subcluster is relocated independently; the formal uncertainty in the location of the hypocentroid for each subcluster is on the order of 1–2 km at a 90 per cent confidence level. The uncertainty of the relative location of each event in the subcluster is added to this base level of location uncertainty to obtain the final estimate of location accuracy. In the entire catalogue of close to 2500 events, horizontal uncertainties average $\pm$ 2.8 km. For events where depth could be constrained (i.e. by near-source readings, teleseismic depth phases or through waveform modelling), uncertainty in focal depth averaged $\pm$ 3–4 km. Relocation vectors are shown in Supporting Information Figs S1–S2.

Results of the relocation procedure are presented in Fig. 3 (see also Supporting Information Figs S10–S14 for cross-sections). As evident in previously published catalogues (Rietbrock *et al.* 2012; Lange *et al.* 2012), our locations indicate several major regions of aftershock activity—outboard of the subduction zone within the oceanic plate, in two distinct clusters along the subduction zone thrust, and within the upper plate surrounding the Pichilemu region, where the 2010 March 11 normal faulting aftershocks occurred. Also evident in map view (e.g. Fig. 3) is the clear change in strike of the aftershock sequence from south to north; from approximately north–south at the southern end of the sequence, to NE-SW in the central portion of the rupture, to north–south again further north; mirroring the changes in strike of the subducting plate over the rupture area of the earthquake. These locations are discussed in more detail in the following section, in conjunction with results from our RMT analysis.

5. RMT ANALYSES

All 2451 well-constrained events, outlined above, were analyzed using a RMT inversion, following the approach of Herrmann *et al.* (2011a). This approach solves for the source depth, moment magnitude, and strike, dip and rake angles of a shear-dislocation source via a time-domain inversion scheme. It assumes a step function in moment release, which is acceptable for smaller earthquakes such as those studied here, where the source corner frequency is greater than the frequencies used for the inversion. Green's functions for IMAD stations (Fig. 1) are computed in a Western United States (WUS) velocity model used in NEIC operations (Herrmann *et al.* 2011a), to remain consistent with NEIC response procedures. The Green's functions were computed using wavenumber integration and represent a complete solution of the elastic wave problem. The inversion process determines the best-fitting RMT solution at 1 km depth intervals over a broad depth range that includes the expected earthquake depth, and permits time shifts to account for slight differences in location and origin time. The use of the WUS
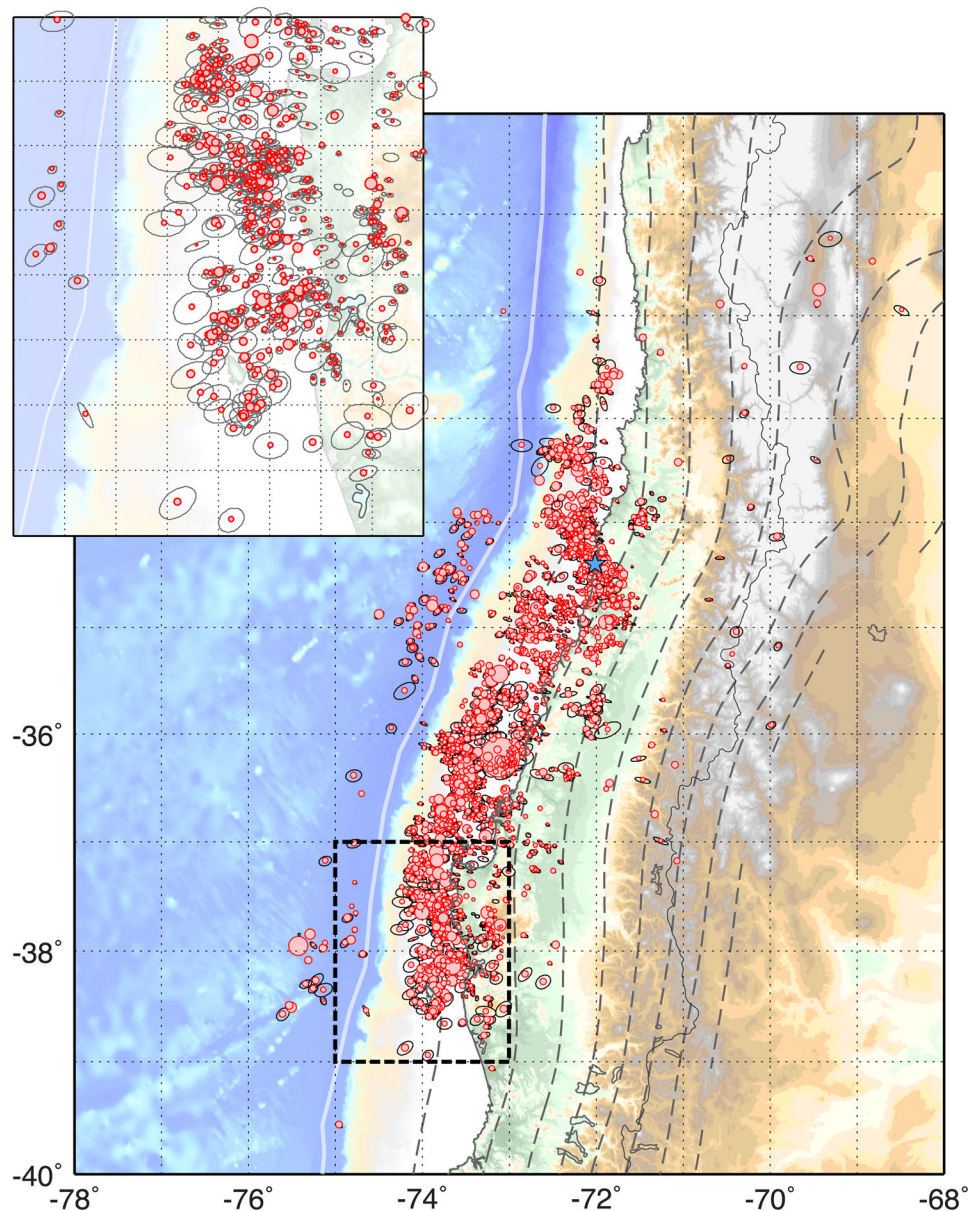
Figure 3. Aftershock relocations, sized by magnitude, and plotted with error ellipses (horizontal uncertainties). Blue star marks the location of Pichilemu, discussed in the text as the location of two large normal faulting aftershocks on 2010 November 03. Inset shows a zoomed region of the southern part of the sequence (black dashed box in main figure), to illustrate details of location uncertainty for the sequence. Dark grey dashed contours represent the depth of the subducting Pacific slab in 20 km intervals, from Slab1.0 (Hayes *et al.* 2012a). The thick transparent white line represents the inferred location of the Nazca: South America Plate boundary.

velocity model was justified by the fact that the predicted wave-forms matched the observed waveforms well in the 0.02–0.06 Hz passband, and by the small time shifts this approach required. Other studies (Herrmann *et al.* 2011b) also found that differences in RMT velocity model primarily influence estimates of the moment magnitude (by approximately 0.1 magnitude units) and RMT depth, but has little influence on the determination of the RMT nodal planes. This is supported by a comparison of a selection of RMT solutions derived using an alternate Eastern United States velocity model (Supporting Information Fig. S3a–c), and by a similar comparison of common RMT solutions between our data set and that of Agurto *et al.* (2012) (Supporting Information Fig. S3d–f). Differences in

strike and dip are typically less than the uncertainties we estimate in our own solutions (below).

For most events, we use a 0.02–0.06 Hz passband, though the high-frequency corner was allowed to vary slightly based on the magnitude of the event. The inversion approach estimates the source depth, moment magnitude, and the strike (ϕ), dip (δ), and rake (λ) angles of a shear-dislocation source. The source time function is assumed to be a step function in moment release, and each event is considered a point source, both acceptable assumptions for the small sized events analyzed here.

We derived 465 RMTS from the data set of 3000+ events analyzed—for this subset of events, IMAD data offered significant
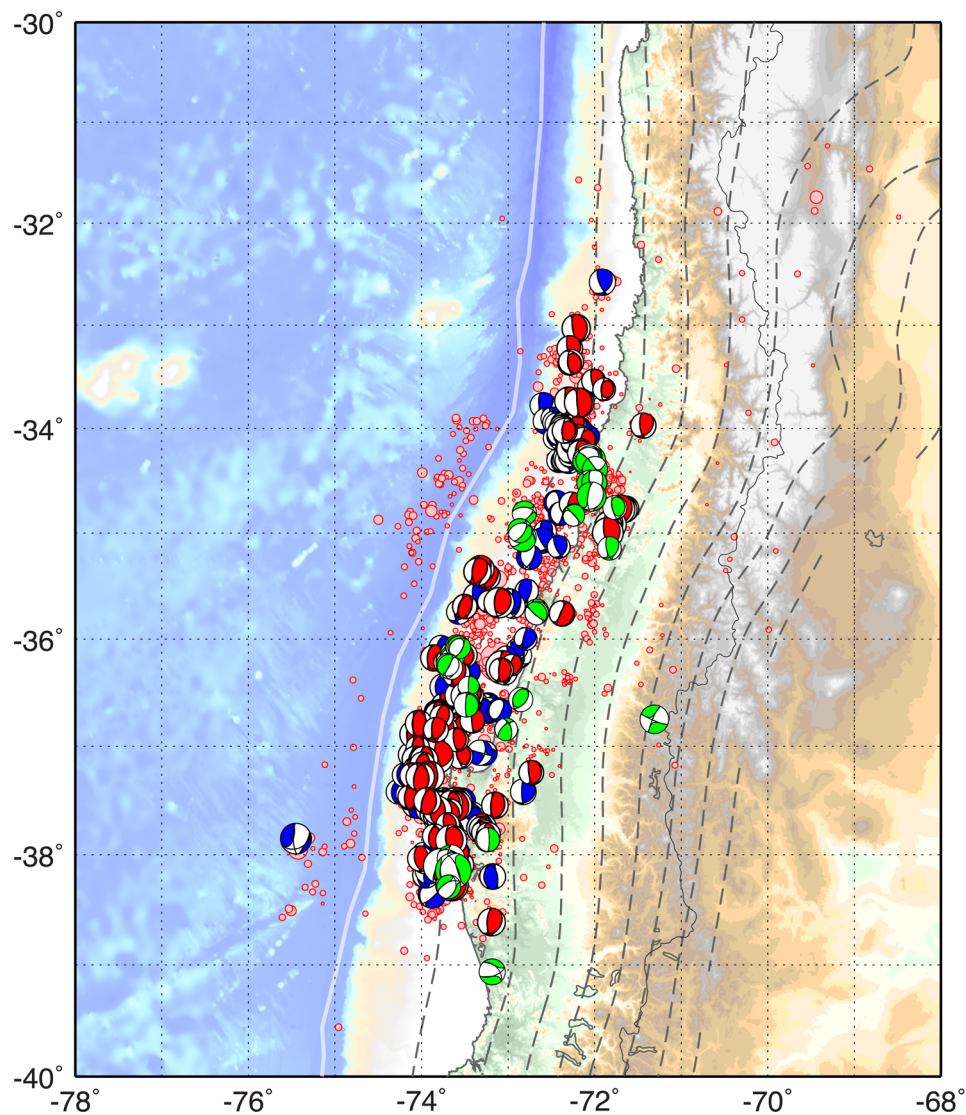
Figure 4. Aftershock relocations and RMTs, subdivided by their inferred tectonic environment (upper, lower, interplate; green, blue, red, respectively). Dark grey dashed contours represent the depth of the subducting Pacific slab in 20 km intervals, from Slab1.0 (Hayes *et al.* 2012a). The thick transparent white line represents the inferred location of the Nazca: South America Plate boundary.

enough azimuthal coverage and waveform quality to give us confidence that our inversion and grid search scheme had produced a source mechanism and hypocentral location that was reasonably well constrained. Quantifying the quality of this constraint is difficult, but very important when using resulting mechanisms to discriminate aftershocks based on tectonic setting. This issue is discussed further in the supplement to this manuscript (Supporting Information Text). Most events had at least one observation within $1°$ of the source (over 60 per cent within $0.5°$), and distance ranges varied between $0°$ and $10°$. Uncertainties in strike and dip have been estimated as $\pm20°$ and $\pm25°$, respectively, though they show some dependence on location and azimuthal gap (Supporting Information Text). The resulting mechanisms are shown in Fig. 4.

As shown in detail by Asano *et al.* (2011), moment tensors for earthquakes in subduction zone settings can be divided into interface, upper and lower plate events through an evaluation of the minimum rotation angle of the moment tensor (also known as 'Kagan's angle'; Kagan 1991) with respect to a reference solution.

The Asano *et al.* (2011) study assumes that small angles of rotation (Kagan's angle $\leq 35°$) for earthquakes close to the assumed slab depth (within 20 km) imply interplate thrusting mechanisms. Non-interplate events are further divided into hanging wall (upper plate) and foot wall (lower plate) events based on whether they are aove or below the slab. We use essentially the same approach here, with one significant modification. The Asano *et al.* (2011) study used a constant reference solution based on the nodal planes of a 'typical' interplate earthquake in their region of interest. Here, we instead use a reference based on the slab geometry at the epicentre of each earthquake (using Slab1.0), thus better accounting for the variations in slab geometry over the region of interest. Such changes can be significant even in the seismogenic zone—for example, in the region of the Maule rupture, slab dip increases from approximately $10°$ in the shallow subduction zone environment, to over $23°$ near the base of the seismogenic zone, at approximately 55 km depth; slab strike varies by as much as $15°$ over the same region. We also explore different approaches to setting the

minimum rotation angle used to distinguish interplate events from lower and upper plate earthquakes. In a first step, we use a value of 35°, as suggested by Asano *et al.* (2011). We compare the results of this approach with a second data set, for which we allow the minimum rotation angle to vary depending on the azimuthal gap of the RMT solution, thus accounting for the location-dependence of the uncertainties in derived mechanisms (Supporting Information Text Section S2). While the first filtering approach likely misclassifies some events in the offshore region, where higher azimuthal gaps in data distributions lead to greater uncertainties in the nodal planes of their RMT solutions and thus interplate earthquake focal mechanisms may appear over-steepened, the second approach leads to a broader range of 'allowable' mechanisms the same classification, thus likely misclassifying some intraplate events as interplate thrust solutions. Comparing both methods allows us to isolate the somewhat ambiguous solutions. This approach leads to a more accurate classification of moment tensors based on their tectonic setting, an analysis we conduct for pre- and post-main shock gCMTs, and the best-constrained aftershock RMTs (Supporting Information Text Section S2).

Prior to the Maule earthquake, the majority of earthquakes with associated moment tensors near the co-seismic rupture zone were thrust faulting, interface-type events (Fig. 2). While the northern part of the rupture area was relatively devoid of moderate-sized earthquakes over the preceding 34 yr, the southern region—between 36°S and 39°S—had hosted ~15 M5–6.6 events at seismogenic depths over the same time period, including a group of 4–5 events clustered within 9–42 km of the main shock hypocentre. Just two upper plate earthquakes occurred in this region over the same time period, near the southern end of the subsequent main shock rupture area, while there were no lower plate earthquakes inboard of the trench large enough to have associated moment tensors.

In contrast, RMTs for the aftershock sequence indicate a broad mixture of faulting styles. Of the highest quality RMT solutions, 53 per cent could be classified as interplate. Of the remaining 47 per cent, 75 per cent (97 events) demonstrate lower plate mechanisms. 12 per cent of the entire RMT data set were upper plate events. Five cross-sections of the aftershock sequence and their RMTs, plotted from the southern end of the source region moving northward, are shown in Supporting Information Figs S10–S14.

RMTs indicate a dominance of thrust faulting close to the subduction zone interface. Cross-sections identify a set of events near the base of the seismogenic zone (e.g. A–A′, B–B′, D–D′) that is spatially distinct from other thrust aftershocks, and helps to define the depth extent of faulting on the plate interface in this region (at the deep limit of these events), as well as the likely depth-extent of co-seismic slip (at the shallow limit of these events). Cross-section D–D′ highlights a sequence of upper plate earthquakes near the northern end of the main shock rupture zone, dominated by normal faulting. These earthquakes are associated with two large M7.0 and M6.9 aftershocks on 2010 March 11 , near Pichilemu. The sequence branches upward from and oblique to the subduction zone interface (strikes of the largest two events are approximately 145° and 155°; www.globalcmt.org), and RMT's align well with the ~145° strike of the inferred main shock fault plane (e.g. Ryder *et al.* 2012), though not all upper plate RMT's demonstrate normal faulting mechanisms; for example, several strike-slip faulting events exist. This upper plate sequence also seems to promote subsequent aftershock activity on the up-dip portion of the megathrust plate boundary (since all RMTs are associated with earthquakes subsequent to the Pichilemu events), while possibly inhibiting activity on the portion of the megathrust directly beneath the upper plate

normal faults where a lack of aftershocks is apparent (Supporting Information Fig. S7). With the exception of much of this Pichilemu cluster, upper and lower intraplate events are dominantly located offshore, particularly in the central and southern regions of the main shock rupture. In the central portion of the rupture, offshore upper and lower plate events cluster between regions of major slip from finite fault modelling (see next section, and Rietbrock *et al.* 2012). Also visible in both cross-section and in map view (Fig. 3) is aftershock activity within the oceanic Nazca Plate outboard of the subduction zone, in two clusters at the northern and southern ends of the main shock rupture. While the more dominant of these clusters, in the north, lies directly up-dip of the main co-seismic asperity, the southern cluster aligns more closely with fracture zones at this end of the rupture, further south than the asperity between 36°S and 37°S.

At the extreme southern end of the rupture, intraplate earthquakes within the slab indicate both normal and oblique thrust faulting. Between 36.5°S and 37.5°S and near 74°W, an extremely interesting cluster of earthquakes imply potential intraplate faulting within the offshore portion of the subducting slab along steep reverse faults. While the mechanisms of these events appear similar to what would be expected for interplate thrusting, the dip angles of the eastward-verging nodal planes are much steeper than the slab dip at the same location—on average rotated over 40° with respect to the interface—greater than the uncertainty in the moment tensor analysis. However, when considering a location-dependent filter for tectonic environment (Supporting Information Text), the larger uncertainties in strike and dip for these events makes it difficult to definitively identify them as lower plate earthquakes. This is to be expected for thrust solutions; thrust faults are inherently low-angle, and so lower plate thrusting events, if they exist, should occur along faults with relatively small rotation angles with respect to the slab interface (less than ~30°). If rotational angles cannot be constrained to within ±40° because of RMT uncertainty (Supporting Information Text), then distinguishing such events from interplate thrusting earthquakes is difficult.

However, these earthquakes may be distinguishable from those located in a similar area, which have been identified as clear interplate events. Since at the same location, RMT uncertainties are approximately equal (if data coverage is similar), differences in RMT's should be the result of real signals. Supporting InformationFig. S15 shows rose diagrams of differences between RMT dips and slab dips for the southern, central and northern sections of the rupture zone. This analysis shows that the steeply rotated events in the south (28°–45° rotation w.r.t. slab surface) are a unique signal in the aftershock sequence, distinct in quantity from similarly steep mechanisms in other parts of the aftershock sequence, and distinct locally from another peak of events classified as interplate because of their lower rotation angles with respect to the slab. With this in mind, we can interpret that some or all of the events in this cluster are representative of a real signal of steep lower plate faulting near the southern end of the main shock rupture. These earthquakes, and other intraplate events further south beneath the shoreline which demonstrate significant rotations in strike with respect to the slab as well as in dip, imply internal deformation of the subducting plate at seismogenic depths. This deformation may occur as a result of intraplate shortening to the south of major interplate moment release, in response to that co-seismic slip. A similar, through less active cluster of lower plate events can be seen in the north near 34°S and between 72°W and 73°W (e.g. Fig. 4, Supporting Information Fig. S7), implying a similar tectonic signal at the northern end of co-seismic rupture.

6. MAIN SHOCK FINITE FAULT ANALYSES

In the hours and days following the Maule earthquake, several different groups published finite fault models describing the slip distribution of this event based on seismic data (e.g. Hayes 2010; Shao *et al.* 2010; Sladen 2010). Since then, many more models have been published with various combinations of seismic, GPS, geologic, tsunami and InSAR data (e.g. Delouis *et al.* 2010; Lay *et al.* 2010; Tong *et al.*, 2010; Lorito *et al.* 2011; Pollitz *et al.* 2011; Vigny *et al.* 2011). Vigny *et al.* (2011) compare how most of these models fit a dense suite of GPS displacement vectors from the epicentral region of the earthquake, collected as both continuous and campaign data. While their model (constructed via an inversion of this same GPS vectors) fits these data best, they show that the USGS model (Hayes 2010) fit the data reasonably well, and better than the other seismic-only models. The majority of the misfit between the Hayes (2010) model and the GPS data comes from a lack of slip in the southern part of the rupture area, also a problem in the other seismic-only solutions.

Vigny et al. (2011) also note a discrepancy between their favoured low-frequency earthquake onset and the USGS-NEIC hypocentre, of approximately 50 km towards the southwest. Rupture velocities for the earthquake were variably reported as 1.75–2.75 km s^{-1} (Hayes 2010); 2.0–2.5 km s^{-1} (Lay *et al.* 2010); averaging 2.6 km s^{-1} but as high as 3.2 km s^{-1} (Delouis *et al.* 2010); and 3.1 km s^{-1} (Vigny *et al.* 2011). Finally, most models used a single-plane geometry for their inversion (with the exception of Lorito *et al.* 2011, and Moreno *et al.* 2012), though some did explore the affect of changing the assumed dip angle for both single (Lay *et al.* 2010; Pollitz *et al.* 2011) and multiple (Lay *et al.* 2010) planes. Each models' geometry was based on approximate fits to the local subduction zone and/or the global CMT solution (www.globalcmt.org; Ekström *et al.* 2012), and varied from 15° to 18° (for single-planes).

In light of these variations and discrepancies, and our own relocations of the hypocentre and aftershocks, we aim to produce an updated slip inversion for the Maule earthquake that fully explores the different assumptions in these previous models. As for the USGS preliminary model (Hayes 2010), we invert only seismic data, utilizing both body and surface waves. In contrast to that model, however, and to the majority of previous inversions discussed above, we explore the effects of better accounting for the variation in slab geometry over the rupture by dividing the model space into several individual planes. We use either three or five planes to match the slab interface. In the three-plane model, we account only for changes in dip, which increases from the trench (10.0°) to the lower limit of the seismogenic zone (23.5°). The hypocentre is located on the middle plane, just offshore, with a dip of 17.5°. For all planes strike is held fixed at 18.7°—the strike of the slab at the hypocentre of the main shock in the USGS Slab1.0 model (Hayes *et al.* 2012). In the five-plane model, we also vary strike, which rotates by approximately 10° in the southern half of the model with respect to the north. Keeping dips the same as in the three-plane model, we shorten fault length along strike and introduce two additional planes south of the hypocentre with strikes of 8.7°, and dips of 10.0° and 17.5°, respectively, matching the upper two planes further north. A sixth plane was not considered necessary, since both single- and three-plane inversions had minimal slip in the southeast corner of the model.

In the three-plane model, each fault is divided into 26 subfaults along strike, and 3 or 4 along dip, for a total of 260 subfaults, 25.00 × 17.75 km in size. In the five-plane model, these planes are shortened to 14 subfaults along strike, and the southerly planes account for an additional 12 subfaults. Fault widths are the same in each model. We follow the approach of Ji *et al.* (2002) to invert for the slip amplitude, direction, rise-time and rupture initiation time of each subfault, where subfault source time functions are modelled with an asymmetric cosine function (Ji *et al.* 2002, 2003), and the velocity model used for Green's function computation is based on a combination of PREM (Dziewonski & Anderson 1981) and Crust 2.0 (Bassin *et al.* 2000).

All models, whether single-plane (Fig. 5), three-plane (Fig. 6), or five-plane (Fig. 7), fit the teleseismic waveform data very well (Supporting Information Figs S16, S18, S20), explaining approximately 88–89 per cent of the waveform data (measured via least-square error between data and synthetics). To compare the model results, we use the geodetic data set presented in Vigny *et al.* (2011), assessing how well each model reproduces the measured static offsets at a large collection of GPS stations (modelled displacements computed using Okada 1992). We quantify the misfit of the predicted offsets to the observations by computing the rms difference between the two vectors (i.e. the root of the sum of the squared lengths of the residual vectors). Results are summarized in Table 1, below, and Supporting Information Figs S17, S19, and S21.

Interestingly, these results show significant improvements in fits of regional GPS data with just stepwise improvements to the assumed fault geometry; data sets and inversion parameters (e.g. rupture velocity, held fixed in the range of 1.5–2.75 km s^{-1}) do not otherwise change for models (i)–(iii) in Table 1. Model (i) improves over model (iv), the original USGS single plane solution (Hayes 2010), by using a refined hypocentral location (relocated 58 km to the SE, at 73.2°W, 36.2°S), via a closer match to the strike and in particular dip of the slab over the earthquake rupture area, and also through the inversion and refined picks of a larger body- and surface-wave data set. The Hayes (2010) model was the best performing of the seismic-only models discussed in Vigny *et al.* (2011), with respect to GPS data. After the Vigny model itself, the best-performing alternate model discussed in Vigny *et al.* (2011) was the Tong *et al.* (2010) inversion, which used InSAR and a selection of GPS data (model (v) above). Our results here suggest that careful consideration of slab geometry can improve seismic data inversions to levels comparable to the lower uncertainties of many inversions based on the local and regional geodetic data, without the specific inclusion of those data in the inversion process. This is a very important observation for the current suite of rapid fault inversion approaches that generally use seismic data alone, before models based on the higher-latency geodetic data become available.

7. COULOMB STRESS TRANSFER MODELLING—SPATIAL DISTRIBUTION OF AFTERSHOCKS AND RMTS

The occurrence of an earthquake—especially one as big as the 2010 Maule event—alters the stress state of surrounding faults and of adjacent areas of the same source fault. Depending on the orientation of these structures with respect to the source, and thus on the sign of the stress change (called the Coulomb failure stress change, ΔCFS; e.g. Stein *et al.* 1997), this can either cause future events on such structures to be advanced or delayed. Thus, if aftershocks are a direct response to co-seismic rupture, and if they are triggered by the static stress changes imparted on their source faults by that main shock rupture, then their locations should be expected to agree with regions of positive ΔCFS (e.g. Lin & Stein 2004).
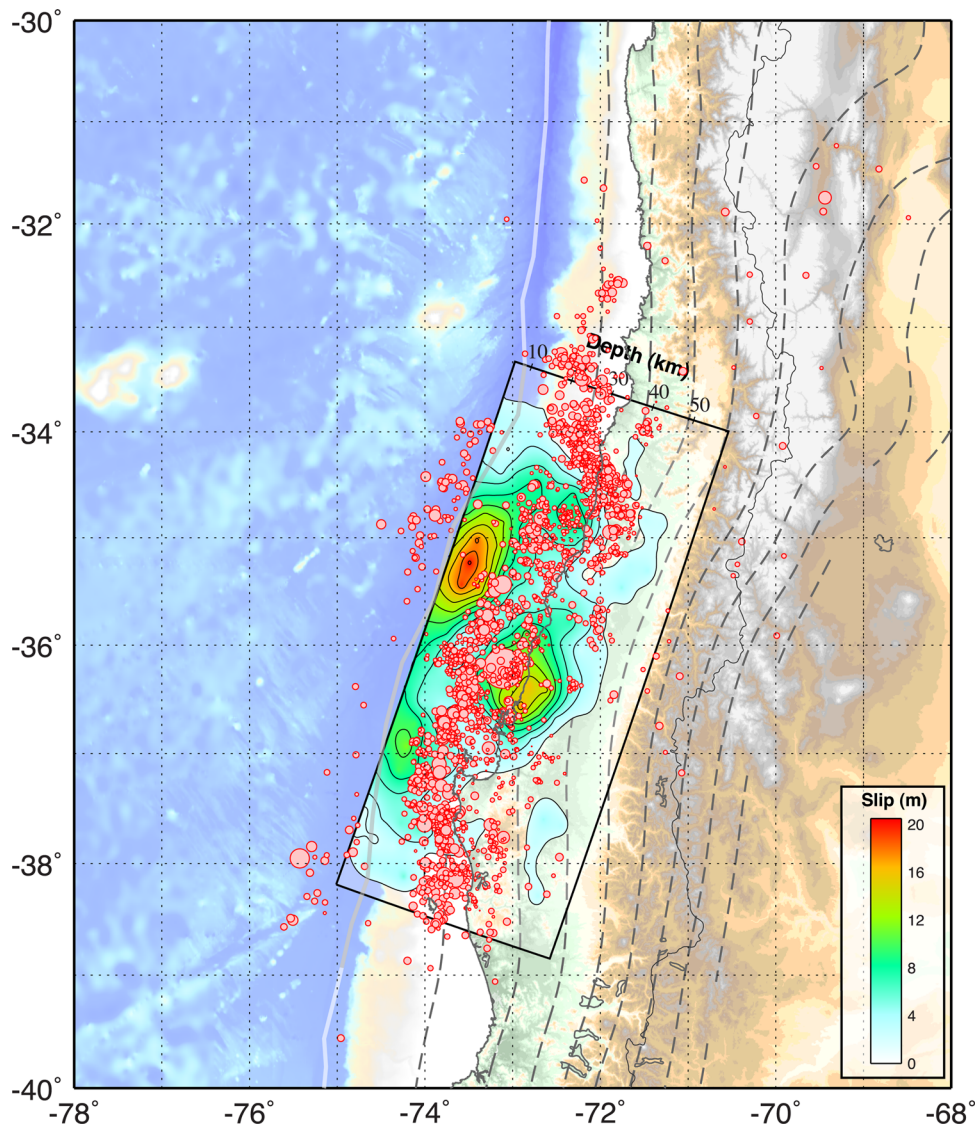
Figure 5. Co-seismic slip model from the inversion of teleseismic data using a single plane (black rectangle encompassing slip distribution) to approximate the subduction zone interface (grey dashed contours, from Slab1.0, Hayes *et al.* 2012). Slip is contoured in 4 m intervals. Overlain on this slip model is the relocated aftershock catalogue, sized by magnitude. The thick transparent white line represents the inferred location of the Nazca: South America Plate boundary.

As shown by Toda *et al.* (2011b), a more rigorous test of the Coulomb hypothesis is to analyze not just the locations of aftershocks with respect to the ΔCFS distribution imparted by the main shock, but to also assess whether the nodal planes of those aftershocks are promoted towards failure. This exercise involves resolving the main shock ΔCFS distribution onto the nodal planes of the aftershock mechanisms, made possible by our extensive RMT catalogue. Furthermore, Toda *et al.* (2011b) showed (as had Hardebeck *et al.* (1998) previously) that in order to demonstrate a causal effect between the main shock ΔCFS distribution and the number of aftershocks brought closer to failure, one must also demonstrate that a similar correlation does not exist with earthquakes in the same region that could not have been triggered by the main shock—i.e. those occurring before the Maule earthquake. In other words, the percentage of positively stressed aftershocks must be normalized by the percentage of positively stressed background earthquakes, providing a percentage gain in positively stressed aftershocks with respect to the control (background) data set.

The Coulomb software package (Toda *et al.* 2005; Toda *et al.* 2011a) has been used to assess these correlations; results are summarized in Table 2. We have analyzed several data sets and slip models. Our control data set of pre-Maule earthquake comes from the gCMT catalogue, and comprises 134 earthquakes that occurred over the same geographical region and depth interval as the aftershocks of the Maule earthquake, over the preceding 34 yr. For post-main shock results, we analyze earthquake data sets from the gCMT catalogue (210 events through 2012 June), and our own relocated RMT catalogue, using both the entire data set (465 events) and those occurring on the subduction zone interface (i.e. for which we can discriminate the likely nodal plane; 235 events).

Results indicate that approximately 57–66 per cent of aftershocks occurred along faults positively stressed by the co-seismic slip of the main shock, depending on the aftershock data set and slip model analyzed (Fig. 8). Furthermore, as much as 55–60 per cent of the control data set occurred along faults brought closer to failure by
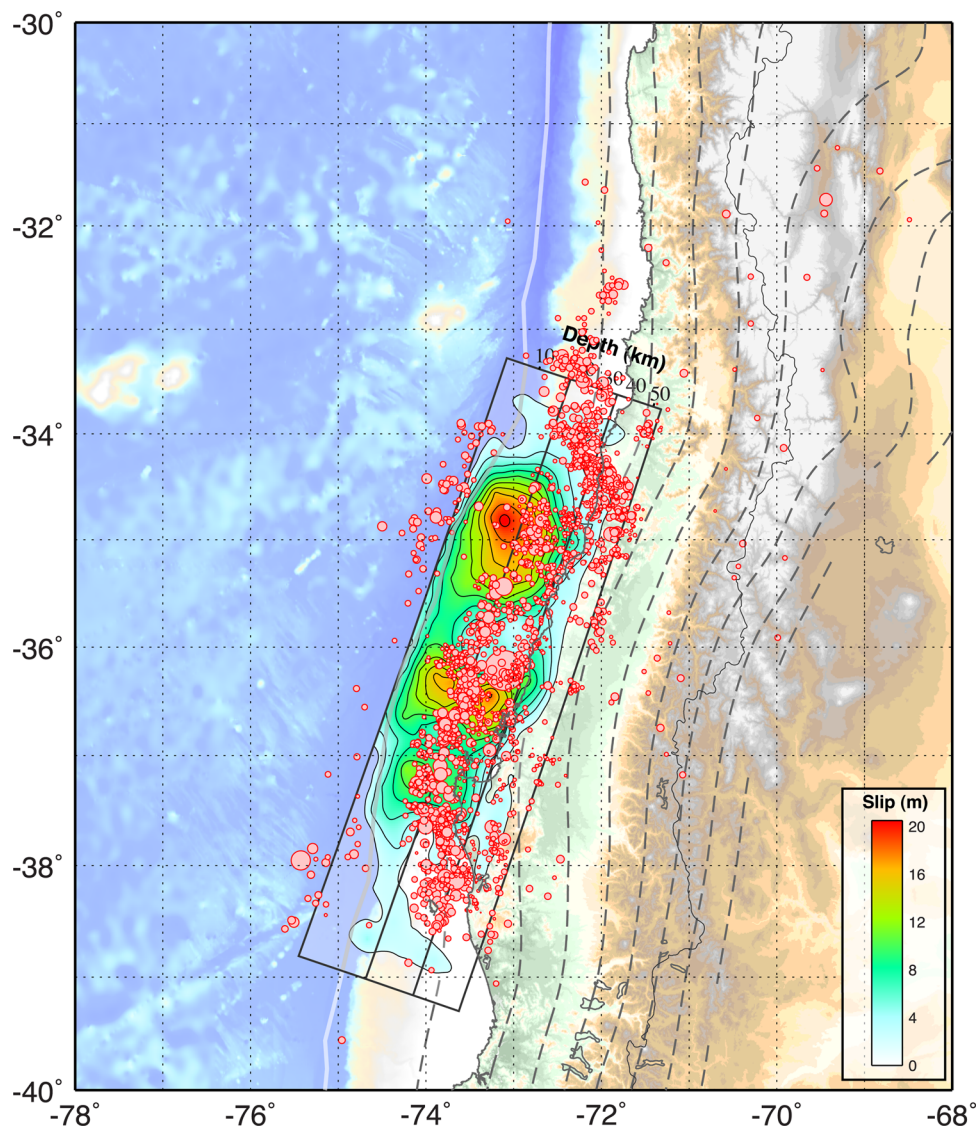
Figure 6. Co-seismic slip model from the inversion of teleseismic data over three planes (black rectangles encompassing slip distribution) approximating the subduction zone interface (grey dashed contours, from Slab1.0, Hayes *et al.* 2012). Slip is contoured in 4 m intervals. Overlain on this slip model is the relocated aftershock catalogue, sized by magnitude. The thick transparent white line represents the inferred location of the Nazca: South America Plate boundary.

the main shock, leading to a gain in the percentage of positively-stressed aftershocks of just 0–14 per cent (as many as 14 per cent more aftershocks are brought closer to failure than the background data set). These numbers compare to mean gains of 47 per cent for the 2011 M 9.0 Tohoku earthquake (Toda *et al.* 2011b), 37–46 per cent for the 1992 M 7.3 Landers earthquake (Hardebeck *et al.* 1998), and 61 per cent for the 1999 M 7.6 Chi-Chi event (Ma *et al.* 2005).

How can we interpret these results? At face value, the number of aftershocks occurring along faults positively stressed by the main shock is not a great deal more than would be expected from a random process. Certainly, the gain of aftershocks brought closer to failure versus background events is very small when compared to previous studies. One potential weakness of our analysis is the relatively small size of the control data set, comprising of just 134 events. Toda *et al.* (2011b) used over 800 mechanisms in their analysis of the Tohoku earthquake. Also, because we have analyzed only the best-recorded events in our relocation procedure, our magnitude of completeness is higher than in other studies (e.g. Ma *et al.* 2005),

meaning we are missing the relatively larger fraction of smaller aftershocks that can provide more detailed information on the spatial pattern of aftershocks (though such locations inherently have higher uncertainties).

Two more insightful tests highlight sensitivities in our results. First, if we consider just those aftershocks occurring outside of the area of the main shock rupture (i.e. those earthquakes surrounding the rupture, rather than contained within it), our percentage gains rise to as high as 67 per cent (Table 2). This implies results are very sensitive to the details of the distribution of slip in the favoured model, and critically the smoothing used in the inversion procedure. Small changes in slip distribution can alter resulting stress distributions at a given aftershock location, such that an event negatively stressed by one model, is positively stressed by another. The effect of such small changes is less apparent further away from the co-seismic slip distribution, hence the relative increase in percentage gain in those regions. This issue thus becomes important for earthquakes with multiple asperities and regions of comparatively low slip between slip highs, as is the case for the Maule earthquake, since
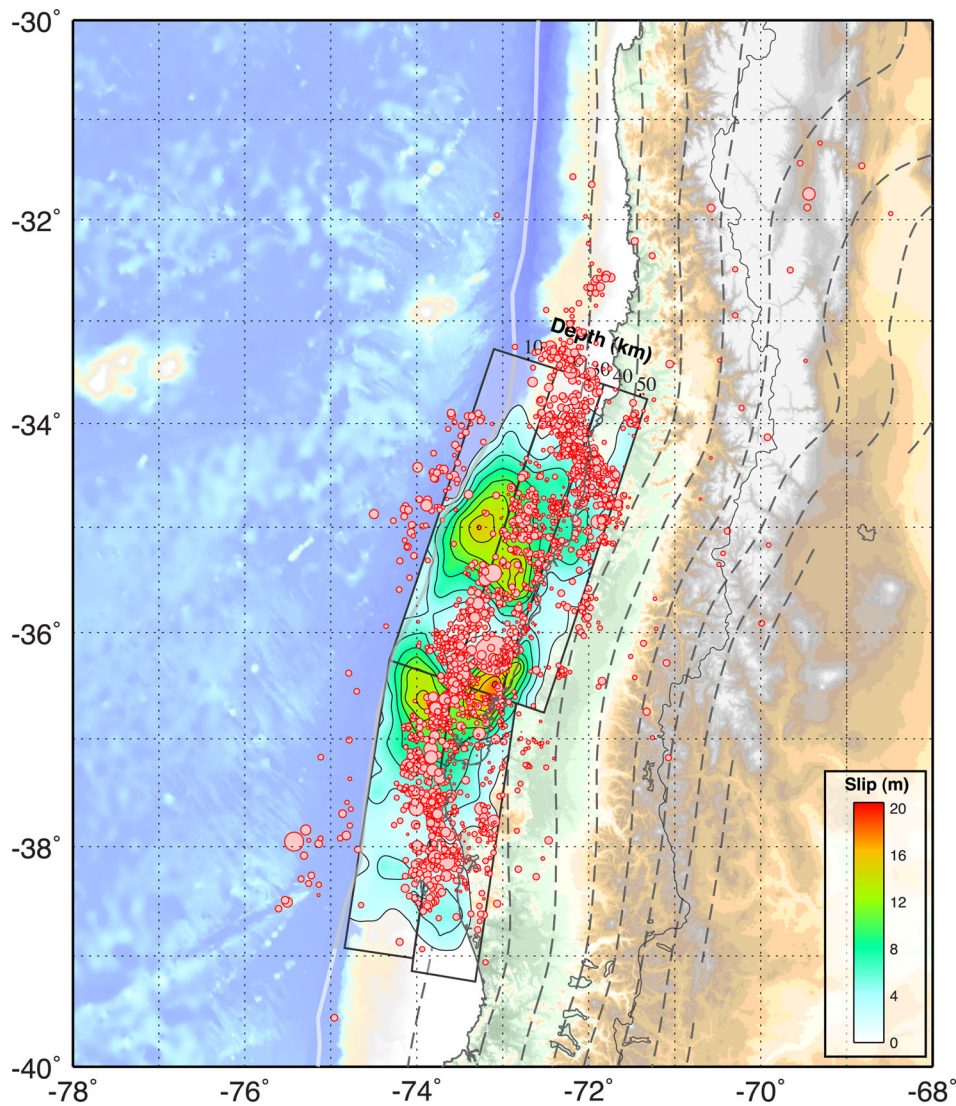
Figure 7. Favoured co-seismic slip model from the inversion of teleseismic data over five planes (black rectangles encompassing slip distribution) approximating the subduction zone interface (grey dashed contours, from Slab1.0, Hayes *et al.* 2012). Slip is contoured in 4 m intervals. Overlain on this slip model is the relocated aftershock catalogue, sized by magnitude. The thick transparent white line represents the inferred location of the Nazca: South America Plate boundary.

aftershocks are likely to occur in the transitional regions between asperities, and thus whether or not their fault planes are modelled to have positive stress changes depends on the relative locations of slip in the co-seismic slip model, and the aftershock hypocentres.

Location uncertainty is therefore a very important issue when assessing Coulomb stress transfer results. Most earthquake catalogue locations have uncertainties as high as several tens of kilometers (Hayes & Wald 2009). The relocated hypocentres considered here have uncertainties on the kilometer scale, averaging less than ± 3 km horizontally. However, even considering just these small horizontal uncertainties and assessing ΔCFS at the bounds of each earthquake's error ellipse, almost 90 per cent of Maule aftershocks are consistent with occurring in regions of positive stress transfer (when compared to the favoured 5-plane slip distribution), implying a percentage gain of as much as 50 per cent over the control data set (Table 2, Fig. 8), almost a factor of ten increase from our analysis considering preferred locations only. This implies we need to have high confidence in the accuracy of both our aftershock data,

Table 1. The rms residuals computed between observed GPS vectors from Vigny *et al.* (2011), and those predicted from finite fault models: (i–iii) in this study, and (iv–vi) a selection of those analyzed in Vigny *et al.* (2011). Bracketed grey values show equivalent rms residuals reported in Vigny *et al.* (2011).

	Model	Horizontal rms (cm)	Vertical rms (cm)
(i)	Single-plane (Fig. 5)	50.05	46.45
(ii)	Three-plane (Fig. 6)	39.63	42.50
(iii)	Five-plane (Fig. 7)	39.72	32.89
(iv)	Hayes (2010)	77.5 (79.54)	33.8 (36.71)
(v)	Tong *et al.* (2010)	32.9	29.3
(vi)	Vigny *et al.* (2011)	16.3	10.7

and our co-seismic slip model, to interpret both as being indicative of support for, or against, the static stress transfer hypothesis. This issue is especially significant for similar studies using preliminary, teleseismic slip models and aftershock locations, which likely

Table 2. Coulomb stress transfer calculations for gCMT and RMT mechanisms, pre- and post-mainshock. Bold numbers indicate calculations excluding all events within the polygon of modeled slip (i.e., those earthquakes surrounding the rupture zone, rather than contained within it; Figs 5–7). Stress effect of mainshock = [100∗(% aftershocks with + ΔCFS/% background with + ΔCFS) − 100]. The last two columns incorporate location uncertainties in the calculations of ΔCFS; if a given earthquake nodal plane is positively stressed at any point within the uncertainty of its' location, it is counted.

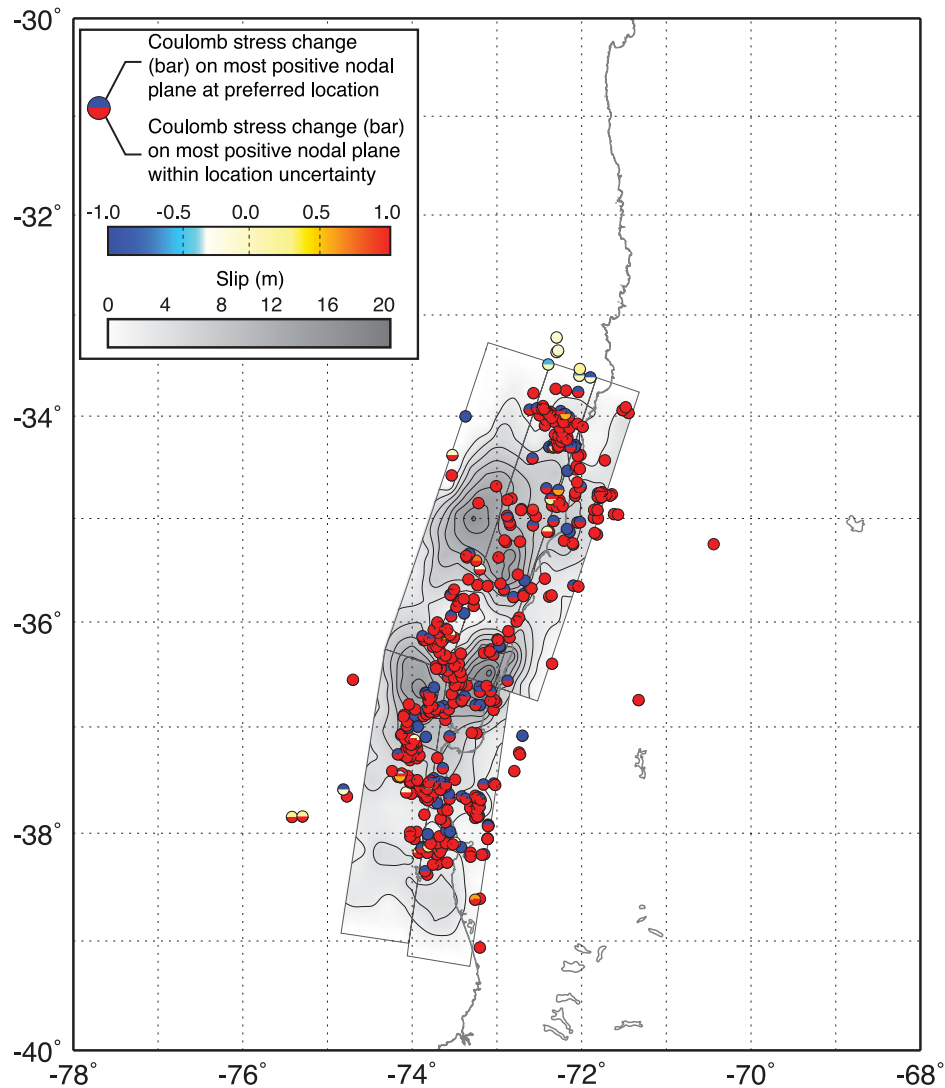| Model	% gCMT aftershocks with + ΔCFS		% RMT aftershocks with + ΔCFS		% RMT-interface aftershocks with + ΔCFS		% background with + ΔCFS		Stress effect of mainshock (% gain)		% aftershocks with + ΔCFS, including location error	% interface aftershocks with + ΔCFS, including location error
SP	58	**83**	57	**75**	60	**70**	59	**55**	−3–2	**27–51**		
3P	58	**79**	66	**84**	63	**83**	58	**61**	0–14	**30–38**		
5P	62	**92**	66	**81**	63	**83**	59	**55**	5–12	**47–67**	87	86

Figure 8. Stress changes resulting from our preferred source model (Fig. 7), resolved on nodal planes of all RMT solutions within the uncertainties of their relocated positions. For non-interplate events, stress change on the most positive nodal plane is shown; for interplate events, stress change is shown resolved onto the shallow, east-verging plane. Each RMT is represented by a circle, whose two colours indicate the maximum stress change at their preferred location (upper hemisphere), and within their location limits (lower hemisphere).

involve much greater uncertainty than the relocated aftershocks and refined slip model used here.

8. SUMMARY

Using data from a regional deployment of seismometers over the rupture area of the 2010 February 27 M_w 8.8 Maule earthquake, in addition to teleseismic data from the largest of these events recorded globally, we have relocated a subset of nearly 2500 aftershocks occurring over the 18 months following the main shock. This catalogue provides calibrated locations accurate to within several kilometers horizontally and vertically for the best-recorded events in the aftershock sequence of this megathrust earthquake.

In addition, we have analyzed the RMTs of close to 500 of these aftershocks, providing more detailed tectonic context for the aftershock sequence than given by hypocentral distributions alone.

These RMTs have been inverted at our calibrated locations, and thus can be interpreted within the same framework as our relocated aftershock catalogue. Together, these data sets provide the first integrated analysis of the aftershock distribution and tectonic framework of the Maule earthquake that can be interpreted in light of their formal location and fault orientation uncertainties.

Using the relocated hypocentre of the main shock, and a systematic analysis of the effects of fault orientation on the slip distribution of the earthquake, we have reanalyzed the teleseismically derived finite fault model for the Maule earthquake. By paying careful attention to data selection, alignments, model parameters, and the orientation of fault planes in the inversion (and specifically how close they match true interface geometry), we are able to show that slip inversions that use only teleseismic data can accurately reproduce co-seismic offsets at regional GPS stations; in other words, careful consideration of slab geometry can improve seismic data inversions to levels comparable to many inversions based on the local and regional geodetic data, without the specific inclusion of those data in the inversion process. Our preferred solution inverts for the co-seismic slip distribution of the Maule earthquake over five adjoining planes that take into account the variation of subduction zone structure both along-dip and along-strike. The model, like many of the other recently published co-seismic slip models (e.g. Moreno *et al.* 2012; Vigny *et al.* 2011), indicates dominantly offshore slip in two-to-three major asperities: north of the hypocentre near 35°S, and in the south near 36°S–37°S. Co-seismic slips reached 15–20 m, and the northern and southern asperities were separated by a prominent minima in slip near the hypocentre, close to the location of the M8.0 1928 megathrust earthquake. Interestingly, while these and other teleseismic and geodetically derived slip models favour slip on the shallower, offshore portions of the subduction thrust, those models including tsunami data (e.g. Lorito *et al.* 2011; Fujii & Satake 2012) derive slip beneath the coastline, somewhat at odds with measurements of coastal subsidence and uplift (Vargas *et al.* 2011). This discrepancy has yet to be satisfactorily resolved.

By comparing our relocated aftershock catalogue to the distribution of slip in this refined finite fault model, we can analyze the relationships between co- and post-seismic slip. Like the Agurto *et al.* (2012) study, our results show that the majority of the interplate after-slip represented by aftershocks occurs away from peaks in co-seismic slip, where slip is either low or relatively moderate with respect to co-seismic maxima. However, comparisons with co-seismic slip gradients (Supporting Information Fig. S22) show that aftershocks do not necessarily occur where changes in co-seismic slip were most rapid; in fact, most aftershocks locate where slip gradients are also moderate-to-low. We also find that overall a smaller fraction of the aftershock sequence is represented by interplate thrusting (55 per cent versus 70 per cent in Agurto *et al.* 2012).

Comparisons of our favoured slip distribution to aftershock focal mechanisms also show that care must be taken when using Coulomb stress transfer calculations to interpret aftershock distributions. Without incorporating uncertainties in aftershock locations, just 55 per cent of aftershock nodal planes align with faults promoted towards failure by co-seismic slip during the main shock. When uncertainties in those locations are considered, 90 per cent of Maule aftershocks are consistent with occurring along faults demonstrating positive stress transfer. With respect to background earthquake rates in the same regions, this amounts to percentage gains of around 10 per cent or 50 per cent, respectively—vastly different results, derived without assessing uncertainties in the spatial pattern of slip from our teleseismic slip model, which are likely larger than those from our relocated aftershocks. As we note, this effect is likely compounded by the complex nature of the slip distribution of the Maule earthquake—because the rupture involved slip over multiple asperities, and aftershocks occurred in regions of low slip between those asperities, Coulomb stress transfer calculations are particularly sensitive to the relative locations of both. The issue would be less apparent in an earthquake with relatively simpler slip, such as the 2011 M_w 9.0 Tohoku earthquake (e.g. Toda *et al.* 2011b). Nevertheless, our results suggest that location uncertainty is an issue that needs to be considered during tests of the Coulomb stress-triggering hypothesis in the future.

REFERENCES

Agurto, H., Rietbrock, A., Ryder, I. & Miller, M., 2012. Seismic-afterslip characterization of the 2010 M_w 8.8 Maule, Chile, earthquake based on moment tensor inversion, *Geophys. Res. Lett.,* **39,** L20303, doi:10.1029/2012GL053434.

Asano, Y., Saito, T., Ito, Y., Shiomi, K., Hirose, H., Matsumoto, T., Aoi, S., Hori, S. & Sekiguchi, S., 2011. Spatial distribution and focal mechanisms of aftershocks of the 2011 off the Pacific Coast of Tohoku Earthquake, *Earth Planets Space,* **63,** 669–673.

Bassin, C., Laske, G. & Masters, G., 2000. The current limits of resolution for surface wave tomography in North America, *EOS Trans AGU,* **81,** Fall Meet. Suppl., Abstract S12A-03.

Beck, S., Barientos, S., Kausel, E. & Reyes, M., 1998. Source characteristics of historic earthquake along the central Chile subduction zone, *J. South Am. Earth Sci.,* **11,** 115–129.

Bondar, I., Bergman, E., Engdahl, E.R., Kohl, B., Kung, Y-L. & McLaughlin, K., 2008. A hybrid multiple event location technique to obtain ground truth event locations, *Geophys. J. Int.,* **175,** 185–201.

Buland, R.P. *et al.*, 2009. Comprehensive seismic monitoring for emergency response and hazards assessment: recent developments at the USGS National Earthquake Information Center, *Eos Trans. AGU,* **90**(52), Fall Meet. Suppl., Abstract S11B-1696.

Campos, J. *et al.*, 2002. A seismological study of the 1835 seismic gap in south-central Chile, *Phys. Earth planet. Inter.,* **132,** 177–195.

Croux, C. & Rousseeuw, P.J., 1992. Time-efficient algorithms for two highly robust estimators of scale, *Comput. Stat.,* **1,** 411–428.

Delouis, B., Nocquet, J-M. & Vallée, M., 2010. Slip distribution of the February 27, 2010 Mw = 8.8 Maule earthquake, central Chile, from static and high-rate GPS, InSAR, and broadband teleseismic data, *Geophys. J. Lett.,* **37,** L17305, doi:10.1029/2010GL043899.

DeMets, C., Gordon, R.G. & Argus, D.F., 2010. Geologically current plate motions, *Geophys. J. Int.,* **181,** 1–80.

Dewey, J.W., 1972. Seismicity and tectonics of western Venezuela, *Bull. seism. Soc. Am.,* **62,** 1711–1751.

Duputel, Z., Rivera, L., Kanamori, H., Hayes, G.P., Hirshorn, B. & Weinstein, S., 2011. Real-time W Phase inversion during the 2011 off the Pacific Coast of Tohoku Earthquake, *Earth Planets Space,* **63,** 535–539.

Duputel, Z., Rivera, L., Kanamori, H. & Hayes, G., 2012. W phase source inversion for moderate to large earthquakes (1990–2010), *Geophys. J. Int.,* **189,** 1125–1147.

Dziewonski, A,M. & Anderson, D.L., 1981. Preliminary reference Earth model, *Phys. Earth planet. Inter.,* **25,** 297–356.

Ekström, G., Nettles, M. & Dziewoński, A.M., 2012. The global CMT project 2004–2010: centroid-moment tensors for 13,017 earthquakes, *Phys. Earth planet. Inter.,* **200–201,** 1–9.

Engdahl, E.R., Van Der Hilst, R.D. & Buland, R.P., 1998. Global teleseismic earthquake relocation with improved travel times and procedures for depth determination, *Bull. seism. Soc. Am.,* **88,** 722–743.

Engdahl, R. & Villaseñor, A., 2002. Global seismicity: 1900–1999, in *International Handbook of Earthquake and Engineering Seismology, Part A*, Chapter 41, pp. 665–690, eds Lee, W.H.K., Kanamori, H., Jennings, P.C. & Kisslinger, C., Academic Press.

Fritz, H.M. *et al.*, 2011. Field survey of the 27 February 2010 Chile Tsunami, *Pure appl. Geophys.,* **168,** 1989–2010.

Fujii, Y. & Satake, K., 2012. Slip distribution and seismic moment of the 2010 and 1960 Chilean earthquakes inferred from tsunami waveforms and coastal geodetic data, *Pure appl. Geophys.,* doi: 10.1007/s00024–012–0524–2.

Ghods, A., Rezapour, M., Bergman, E., Mortezanejad, G. & Talebian, M., 2012. Relocation of the 2006 Mw 6.1 Silakhour, Iran, earthquake sequence: details of fault segmentation on the Main Recent fault, *Bull. seism. Soc. Am.,* **102,** 398–416.

Hardebeck, J.L., Nazareth, J.J. & Hauksson, E., 1998. The static stress change triggering model: constraints from two southern California aftershock sequences, *J. geophys. Res.,* **103,** 24 427–24 437.

Hayes, G., 2010. Finite fault model, updated results of the Feb. 27, 2010 Mw 8.8 Maule, Chile earthquake. Available at: http://earthquake.usgs.gov/earthquakes/eqinthenews/2010/us2010tfan/finite_fault.php. (last accessed July 30 2013)

Hayes, G.P., 2011. Rapid source characterization of the 2011 Mw 9.0 off the Pacific coast of Tohoku earthquake, *Earth Planets Space,* **63,** 529–534.

Hayes, G.P. & Wald, D.J., 2009. Developing framework to constrain the geometry of the seismic rupture plane in subduction zones a priori—a probabilistic approach, *Geophys. J. Int.,* **176,** 951–964.

Hayes, G.P., Rivera, L. & Kanamori, H., 2009. Source inversion of the W-Phase: real- time implementation and extension to low magnitudes. *Seismol. Res. Lett.,* **80,** 817–822.

Hayes, G.P., Earle, P.S., Benz, H.M, Wald, D.J. & Briggs, R.W. the USGS/NEIC Earthquake Response Team, 2011. 88 Hours: The U.S. Geological Survey National Earthquake Information Center reponse to the 11 March 2011 Mw 9.0 Tohoku earthquake, *Seismol. Res. Lett.,* **82,** 481–493.

Hayes, G.P., Wald, D.J. & Johnson, R.L., 2012. Slab1.0: a three-dimensional model of global subduction zone geometries, *J. geophys. Res.,* **117,** B01302, doi:10.1029/2011JB008524.

Herrmann, R.B., Benz, H. & Ammon, C.J., 2011a. Monitoring the earthquake source process in North America, *Bull. seism. Soc. Am.,* **101,** 2609–2625.

Herrmann, R.B., Malagnini, L. & Munafo, I., 2011b. Regional moment tensors of the 2009 L'Aquila earthquake sequence, *Bull. seism. Soc. Am.,* **101,** 975–993.

Ji, C., Wald, D.J. & Helmberger, D.V., 2002. Source description of the 1999 Hector Mine, California, earthquake, part I: wavelet domain inversion theory and resolution analysis, *Bull. seism. Soc. Am.,* **92,** 1192–1207.

Ji, C., Helmberger, D.V., Wald, D.J. & Ma, K.-F., 2003. Slip history and dynamic implications of the 1999 Chi-Chi, Taiwan, earthquake, *J. geophys. Res.,* **108,** doi:10.1029/2002JB001764.

Jordan, T.H. & Sverdrup, K.A., 1981. Teleseismic location techniques and their application to earthquake clusters in the South-Central Pacific, *Bull. seism. Soc. Am.,* **71,** 1105–1130.

Kagan, Y., 1991. 3-D rotation of double-couple earthquake sources, *Geophys. J. Int.,* **106,** 709–716.

Kanamori, H. & Rivera, L., 2008. Source inversion of W phase: speeding up seismic tsunami warning. *Geophys. J. Int.,* **175,** 222–238.

Kennett, B.L.N., Engdahl, E.R. & Buland, R., 1995. Constraints on seismic velocities in the Earth from traveltimes, *Geophys. J. Int.,* **122,** 108–124.

Lange, D. *et al.*, 2012. Aftershock seismicity of the 27 February 2010 Mw 8.8 Maule earthquake rupture zone, *Earth planet. Sci. Lett.,* **317–318,** 413–425.

Lay, T., Ammon, C.J., Kanamori, H., Koper, K.D., Sufri, O. & Hutko, A.R., 2010. Teleseismic inversion for rupture process of the 27 February 2010 Chile (Mw 8.8) earthquake, *Geophys. J. Lett.,* **37,** L13301, doi:10.1029/2010GL043379.

Lin, J. & Stein, R.S., 2004. Stress triggering in thrust and subduction earthquakes, and stress interaction between the southern San Andreas and nearby thrust and strike- slip faults, *J. geophys. Res.,* **109,** doi:10.1029/2003JB002607.

Lorito, S. *et al.*, 2011. Limited overlap between the seismic gap and coseismic slip of the great 2010 Chile earthquake, *Nature Geo.,* **4,** doi: 10.1038/NGEO1073.

Ma, K-F., Chan, C-H. & Stein, R.S., 2005. Response of seismicity to Coulomb stress triggers and shadows of the 1999 Mw = 7.6 Chi-Chi, Taiwan, earthquake, *J. geophys. Res.,* **110,** doi:10.1029/2004JB003389.

McCann, W.R., Nishenko, S.P., Sykes, L.R. & Krause, J., 1979. Seismic gaps and plate tectonics: seismic potential for major boundaries. *Pure appl. Geophys.,* **117**(6), 1082–1147.

Moreno, M., Rosenau, M. & Oncken, O., 2010. 2010 Maule earthquake slip correlates with pre-seismic locking of Andean subduction zone, *Nature,* **467,** doi:10.1038/nature09349.

Moreno, M. *et al.*, 2012. Toward understanding tectonic control on the Mw 8.8 2010 Maule Chile earthquake, *Ear. Planet. Sci. Lett.,* **321–322,** 152–165.

Okada, Y., 1992. Internal deformation due to shear and tensile faults in a half-space, *Bull. seism. Soc. Am.,* **82**(2), 1018–1040.

Pollitz, F. *et al.*, 2011. Coseismic slip distribution of the February 27, 2010 Mw 8.8 Maule, Chile earthquake, *Geophys. Res. Lett.,* **38,** L09309, doi:10.1029/2011GL047065.

Rietbrock, A., Ryder, I., Hayes, G., Haberland, C., Comte, D., Roecker, S. & Lyon-Caen, H., 2012. Aftershock seismicity of the 2010 Maule Mw = 8.8, Chile, earthquake: correlation between co-seismic slip models and aftershock distribution?, *Geophys. Res. Lett.,* **39,** L08310, doi:10.1029/2012GL051308.

Rodi, W., Engdahl, E.R., Bergman, E.A., Waldhauser, F., Pavlis, G.L., Israelsson, H., Dewey, J.W. & Toksöz, M.N., 2002. A new grid-search multiple-event location algorithm and a comparison of methods, *Proceedings of the 24th Seismic Research Review—Nuclear Explosion Monitoring: Innovation and Integration,* pp. 403–411.

Ruegg, J.C. *et al.*, 2009. Interseismic strain accumulation measured by GPS in the seismic gap between Constitución and Concepción in Chile, *Phys. Earth planet. Inter.,* **175,** 78–85.

Ryder, I., Rietbrock, A., Kelson, K., Bürgmann, R., Floyd, M., Socquet, A., Vigny, C. & Carrizo, D., 2012. Large extensional aftershocks in the continental forearc triggered by the 2010 Maule earthquake, Chile, *Geophys. J. Int.,* **188,** 879–890.

Shao, G., Li, X., Liu, Q., Zhao, X., Yano, T. & Ji, C. Preliminary slip model of the Feb 27, 2010 Mw 8.9 Maule, Chile Earthquake. Available at: http://www.geol.ucsb.edu/faculty/ji/big_earthquakes/2010/02/27/chile_2_27.html. (last accessed July 30 2013)

Sladen, A., 2010. Preliminary result 02/27/2010 (Mw 8.8), Chile. Available at: http://tectonics.caltech.edu/slip_history/2010_chile/index.html. (last accessed July 30 2013)

Stein, R.S., Barka, A.A. & Dieterich, J.H., 1997. Progressive failure on the North Anatolian fault since 1939 by earthquake stress triggering, *Geophys. J. Int.,* **128,** 594–604.

Tatar, M., Jackson, J., Hatzfeld, D. & Bergman, E., 2007. The 2004 May 28 Baladeh earthquake (Mw 6.2) in the Alborz, Iran: overthrusting the South Caspian Basin margin, partitioning of oblique convergence and the seismic hazard of Tehran, *Geophys. J. Int.,* **170,** 249–261.

Toda, S., Stein, R.S., Sevilgen, V. & Lin, J., 2011a. Coulomb 3.3, graphic-rich deformation and stress change software, application and 40 p. User Guide, *U.S. Geol. Surv. Open File Rep.,* 2011–1060.

Toda, S., Lin, J. & Stein, R.S., 2011b. Using the 2011 Mw 9.0 off the Pacific coast of Tohoku Earthquake to test the Coulomb stress triggering hypothesis and to calculate faults brought closer to failure, *Earth Planets Space,* **63,** 725–730.

Toda, S., Stein, R. S., Richards-Dinger, K. & Bozkurt, S., 2005. Forecasting the evolution of seismicity in southern California: animations built on earthquake stress transfer, *J. geophys. Res.,* B05S16, doi:10.1029/2004JB003415.

Tong, X. *et al.*, 2010. The 2010 Maule Chile earthquake: downdip rupture limit revealed by space geodesy, *Geophys. Res. Lett.,* **37,** L24311, doi:10.1029/2010GL045805.

Vargas, G., Farías, M., Carretier, S., Tessara, A., Baize, S. & Melnick, D., 2011. Coastal uplift and tsunami effects associated to the 2010 M$_w$ 8.8 Maule earthquake in Central Chile, *Andean Geol.,* **38**(1), 219–238.

Vigny, C. *et al.*, 2011. The 2010 *M*w 8.8 maule megathrust earthquake of central chile, monitored by GPS, *Science,* **332,** doi:10.1126/science.1204132.

Waldhauser, F. & Ellsworth, W.L., 2000. A double-difference earthquake location algorithm: method and application to the northern Hayward fault, California, *Bull. seism. Soc. Am.,* **90,** 1353–1368.

Walker, R.T., Bergman, E., Jackson, J., Ghorashi, M. & Talebian, M., 2005. The 2002 June 22 Changureh (Avaj) earthquake in Qazvin province, northwest Iran: epicentral relocation, source parameters, surface deformation and geomorphology, *Geophys. J. Int.,* **160,** 707–720.

Walker, R.T., Bergman, E.A., Szeliga, W. & Fielding, E.J., 2011. Insights into the 1968–1997 Dasht-e-Bayaz and Zirkuh earthquake sequences, eastern Iran, from calibrated relocations, InSAR and high-resolution satellite imagery, *Geophys. J. Int.,* **187,** 1577–1603.

SUPPORTING INFORMATION

Additioal Supporting Information may be ound in the online version of this article:

Figure S1: Relocation vectors of the Maule aftershock sequence. Relocation shifts to final locations (red circles) are shown with black lines. Light grey dashed contours represent the depth of the subducting Pacific slab in 20 km intervals, from Slab1.0 (Hayes *et al.* 2012). The thick transparent white line represents the inferred location of the Nazca: South America Plate boundary.

Figure S2: Rose diagram views of the Maule aftershock relocation vectors. In (a), we show the length and azimuth of each relocation vector; (b) shows a polar histogram of all vectors, in 5° bins.

Figure S3: Variation in RMT solutions caused by changes in velocity model (a–c), and methodology (d–f). In (a–c), we compare RMT solutions for a random subset of events using our preferred Western United States velocity model, with solutions for the same events derived with an Eastern United States velocity model. In (d–f), we compare solutions for common events in this study with those of Agurto *et al.* (2012). In all cases, differences are less than the uncertainties estimated for our own RMT analysis.

Figure S4: Variation of RMT goodness of fit with strike, relative to the RMS and strike of the best-fit solution. To compute each fit value, strike is varied in 1° increments while holding other fault plane parameters fixed. 4 plots are shown; in (a), events with rms > 0.8 (13 events); (b), 0.8 > rms > 0.7 (58 events); (c), 0.7 > rms > 0.6 (141 events); (d), 0.5 > rms > 0.5 (73 events). Each grey line represents the fit function for an individual event; red lines are averages over all events in each bin. Green lines represent the associated range in acceptable solutions, corresponding to those solutions whose rms is 90 per cent or more of the best-fit value.

Figure S5: Variation of RMT goodness of fit with dip, relative to the rms and dip of the best-fit solution. See Fig. S4 caption for details of panels and symbology.

Figure S6: Azimuthal gap dependent rotation angle uncertainty, derived from an analysis of how uncertainties in RMT solutions affect moment tensor rotation angles, and how these uncertainties vary with the azimuthal gap in data coverage for a given RMT solution (a proxy for RMT location). The red line shows the relationship derived via linear regression; the black dashed line shows the suggested rotational angle used by Asano *et al.* (2011).

Figure S7: Regional moment tensor tectonic classifications. For well-constrained moment tensors, panels (a), (d) and (g) show upper plate events (green); (b), (e) and (h) interplate (red), and (c), (f) and (i) lower plate (blue). As discussed in the Supporting Information text, we follow three approaches of classification. The first (panels a–c) assumes events with rotation angles with respect to the slab of greater than 35° are upper or lower plate events. In a second approach (panels d–f), we develop a location-dependent filter, in which this minimum rotation angle varies with location according to azimuthal gap (Fig. S6). In a third approach (panels g–i), we merge the previous two, using a location-dependent filter for minimum rotation angle that cannot be lower than 35°.

Figure S8: Regional moment tensor tectonic classifications for poorly constrained moment tensors. See caption to Fig. S7 for details. Here, dark green, orange and light blue moment tensors are upper, inter and lower plate events, respectively.

Figure S9: Differences between each approach of tectonic classification. In (a), moment tensors are those well-constrained solutions that are different in approach 2 (variable rotation angle) with respect to approach 1 (fixed rotation angle, 35°). In (b), moment tensors are those well-constrained solutions that are different in approach 3 (variable rotation angle, minimum 35°) with respect to approach 1. In (c), moment tensors are those well-constrained solutions that are different in approach 3 with respect to approach 2. Panels (d)–(f) show the same comparisons for poorly constrained solutions. Green/dark-green moment tensors are upper-plate solutions, red/orange interplate, and blue/light-blue lower plate.

Figure S10: Cross-section A-A′ through the aftershock sequence showing the depth distribution of historic (light grey circles, thin black outlines) and relocated aftershock (dark grey circles, red outlines) seismicity, with symbols sized according to magnitude. For cross-section locations, see Fig. S1. RMTs of the aftershock sequence are also shown, as rear-hemisphere projections of the best fitting double-couple mechanism, subdivided by their inferred tectonic environment (upper-, inter- lower-plate; green, blue, red; in (a), (d), and (f), respectively). Red dashed lines show the subduction zone interface location, from Slab1.0 (Hayes *et al.* 2012a). The black solid line near the surface shows bathymetry/topography, taken from GEBCO bathymetric data. Panels (b), (e) and (g) show the angular rotation of each RMT mechanism from the subduction zone interface at the same horizontal location along the cross-section. Small angles (<~35°, blue-white) align closely with the interface; large angles (>~35°, white-red) do not. Panel (c) shows the approximate moment distribution of interplate aftershocks per kilometer along the dip direction of the subduction zone (red line with grey shading), versus co-seismic slip (grey line). Light grey lines are slices through the favoured co-seismic slip model (figure 7) every 2 km along strike over the ± 50 km width of the cross-section. Dark grey line is the slice in the middle of the section, and the dashed blue line is the average of all slices.

Figure S11: Cross-section B–B′. See caption to Fig. S10 for details of panels and symbology.

Figure S12: Cross-section C–C′. See caption to Fig. S10 for details of panels and symbology.

Figure S13: Cross-section D–D′. See caption to Fig. S10 for details of panels and symbology.

Figure S14: Cross-section E–E′. See caption to Fig. S10 for details of panels and symbology.

Figure S15: Rose diagrams of RMT rotations with respect to the local slab surface. In (a), (c) and (e), we show rotations in the shallow east-dipping plane of each RMT with respect to the slab for events in the north, central, and southern parts of the aftershock sequence, respectively. Grey shading represent all events in each region; blue shaded bars represent those interpreted as lower-plate earthquakes. In (b), (d) and (f), we show full rotation angles of each RMT moment tensor with respect to the slab for events in the north, central, and southern parts of the aftershock sequence, respectively. The black dashed line at 35° marks the cutoff between interplate and upper/lower plate events suggested by Asano *et al.* (2011).

Figure S16: Seismic waveform fits for the single-plane finite fault model (Fig. 5), for (a) P-, SH-, and (b) long-period (vertical, Z, and horizontal, T) data. Relative weights are represented by thickness (e.g. transverse (T) component of station FDF) of data (black) and synthetics (red). Numbers at the beginning of each record represent distance (in degrees, bottom) and azimuth (in degrees, top) to station, while numbers at the end of each record represent the peak amplitude of the data.

Figure S17: Observed and computed static displacement field using the single-plane finite fault model (figure 5). Horizontal vectors are shown in red, vertical in blue, for observations (a), model predictions (b), and residuals (c). Mean horizontal and vertical residuals are 50.1 cm and 46.5 cm, respectively.

Figure S18: Seismic waveform fits for the three-plane finite fault model (figure 6), for (a) P-, SH-, and (b) long-period (vertical, Z, and horizontal, T) data. Relative weights are represented by thickness (e.g. transverse (T) component of station FDF) of data (black) and synthetics (red). Numbers at the beginning of each record represent distance (in degrees, bottom) and azimuth (in degrees, top) to station, while numbers at the end of each record represent the peak amplitude of the data.

Figure S19: Observed and computed static displacement field using the three-plane finite fault model (figure 5). Horizontal vectors are shown in red, vertical in blue, for observations (a), model predictions (b), and residuals (c). Mean horizontal and vertical residuals are 39.6 and 42.5 cm, respectively.

Figure S20: Seismic waveform fits for the favoured, five-plane finite fault model (Fig. 7), for (a) P-, SH-, and (b) long-period (vertical, Z, and horizontal, T) data. Relative weights are represented by thickness (e.g. transverse (T) component of station FDF) of data (black) and synthetics (red). Numbers at the beginning of each record represent distance (in degrees, bottom) and azimuth (in degrees, top) to station, while numbers at the end of each record represent the peak amplitude of the data.

Figure S21: Observed and computed static displacement field using the favoured five-plane finite fault model (figure 5). Horizontal vectors are shown in red, vertical in blue, for observations (a), model predictions (b), and residuals (c). Mean horizontal and vertical residuals are 39.7 cm and 32.9 cm, respectively.

Figure S22: For each slip model (i)–(iii) (Figs 5–7), (a) compares interplate aftershocks (Fig. 4) to normalized slip, and (b) to normalized slip gradient (http://gji.oxfordjournals.org/lookup/supp1/doi:10.1093/gji/ggt238/-/DC1).

Please note: Oxford University Press is not responsible for the content or functionality of any supporting materials supplied by the authors. Any queries (other than missing material) should be directed to the corresponding author for the article.